Dissolution–precipitation processes governing the carbonation and silicification of the serpentinite sole of the New Caledonia ophiolite

Marc Ulrich, Manuel Muñoz, Stéphane Guillot, Michel Cathelineau, Christian Picard, Benoit Quesnel, Philippe Boulvais, Clément Couteau

Dissolution-precipitation processes governing the carbonation and silicification of the serpentinite sole of the New Caledonia Ophiolite

Marc Ulrich[1,2,#,*], Manuel Muñoz[2], Stéphane Guillot[2], Michel Cathelineau[1], Christian Picard[3], Benoit Quesnel[4], Philippe Boulvais[4], Clément Couteau[5].

[1] *Laboratoire Géoressources, CNRS, UMR 7566 , Université de Lorraine, France.*

[2] *Institut des Sciences de la Terre, CNRS, UMR 5275, Université de Grenoble 1, France.*

[3] *Laboratoire Chrono-environnement, UMR 6249, Université de Franche-Comté, France.*

[4] *Géosciences Rennes, CNRS, UMR 6118, Université de Rennes 1, France.*

[5] *Service géologique, Koniambo Nickel SAS, Nouvelle Calédonie.*

[#] *present location: IPGS-EOST, UMR 7516, Université de Strasbourg, France*

[*] *corresponding author: mulrich@unistra.fr*

ABSTRACT

The weathering of mantle peridotite tectonically exposed to the atmosphere leads commonly to natural carbonation processes. Extensive cryptocrystalline magnesite veins and stock-work are widespread in the serpentinite sole of the New Caledonia ophiolite. Silica is systematically associated with magnesite. It is commonly admitted that Mg and Si are released during the laterization of overlying peridotites. Thus the occurrence of these veins is generally attributed to a *per descensum* mechanism that involves the infiltration of meteoric waters enriched in dissolved atmospheric CO_2. In this study we investigate serpentinite carbonation processes, and related silicification, based on a detailed petrographic and crystal-chemical study of serpentinites. The relationships between serpentine and alteration products are described using an original method for the analysis of µ-XRF images performed at the centimeter scale.

Our investigations highlight a carbonation mechanism, together with precipitation of amorphous silica and sepiolite, based on a dissolution-precipitation process. In contrast with the *per descensum* Mg/Si-enrichment model that is mainly concentrated in rock fractures, dissolution-precipitation process is much more pervasive. Thus, although the texture of rocks remains relatively preserved, this process extends more widely into the rock, and may represent a major part of total carbonation of the ophiolite.

Keywords: Serpentine, magnesite, carbonation, silicification, New Caledonia ophiolite

INTRODUCTION

Carbon dioxide is currently one of the primary greenhouse gases having an impact on global warming. Therefore, numerous recent studies have focused on the potential of sequestration of CO_2 by mineral carbonation, either through *ex situ* (*e.g.* Bobicki *et al.*, 2011; Power *et al.,* 2011; Renforth *et al.*, 2011; Badlucan and Dlugogorski, 2013; Harrison *et al.*, 2013) or *in situ* processes (*e.g.* Cipolli *et al.*, 2004; Hansen *et al.,* 2005; Teir *et al.,* 2007; 2009; Andreani *et al.*, 2009; Rudge *et al.*, 2010; Kelemen *et al.*, 2011; Klein and Garrido, 2011). Among the various mineral species that may undergo carbonation reaction, Mg-bearing minerals (as well as Ca-carbonates) are of a great interest as they are very common at Earth surface and thus represent an important reservoir for CO_2. In addition, magnesite ($MgCO_3$) has a long term stability, contrarily to alkali carbonates, which are readily soluble in water (Lackner *et al.*, 1995). Basically, magnesite is formed by the reaction between a Mg-rich source and CO_2-rich fluids (Bain, 1924) and can integrate variable amount of cations (mainly divalent, *e.g.* Ca and Fe) by substituting Mg in the crystal structure. Based on the study of numerous magnesite deposits, Abu-Jaber and Kimberley (1992b) distinguished vein-type and massive-type magnesite, the second type forming deeper than the former. Numerous other parameters play a role in magnesite formation, such as temperature, the origin of the components or the mechanisms of precipitation. The temperature of magnesite formation extends from ambient to ~400°C (Halls and Zhao, 1995; Wilson *et al.*, 2009; Klein and Garrido, 2011). The origin of CO_2 is variable as it may be related to either weathering (atmospheric CO_2), metamorphic (deep seated CO_2) or magmatic (magmatic CO_2) sources (Abu-Jaber and Kimberley, 1992b). The source of magnesium is usually local at the outcrop scale but can also be distant, *e.g.* coming from the weathering of magnesian rocks at the Earth surface and transported downward by meteoric water infiltration (Podwojewski, 1995; Jurković *et al.*, 2012). Mechanisms of magnesite precipitation are also variable. Abu-Jaber and Kimberley (1992b) reported two main ways of magnesite precipitation: i) precipitation through a reaction that involves CO_2-rich fluid and Mg-rich rock, or alternatively Mg-rich fluids and CO_2-rich rock (*i.e.* the most common way to form magnesite); ii) the oversaturation of the fluid with respect to magnesite may be enhanced by the fluid evaporation and/or degassing (Dabitzias, 1980; Fallick *et al.*, 1991; Zedef *et al.*, 2000; Ghoneim *et al.*, 2003). In both cases, hydrated Mg-carbonate species may precipitate alternatively or in association to magnesite (*e.g.* Zedef *et al.*, 2000; Beinlich and Austrheim, 2012) Detailed studies of the precipitation mechanisms can thus provide major clues for the understanding of natural CO_2 sequestration.

Among the various rocks that have the potential to react with CO_2, ultramafic rocks, and particularly serpentinites, are probably the most efficient feedstock material for long-time storage through the formation of magnesite (Dabitzias, 1980; Jedrysek and Halas, 1990; Pohl, 1990; Fallick *et al.*, 1991; Abu-Jaber and Kimberley, 1992b; Sherlock and Logan, 1995; Goff and Lackner, 1998; Gerdemann *et al.*, 2003; Ghoneim *et al.*, 2003; Cipolli *et al.*, 2004; Schulze *et al.*, 2004; Hansen *et al.*, 2005; Teir *et al.*, 2007, 2009; Kelemen and Matter, 2008; Rudge *et al.*, 2010; Klein and Garrido, 2011; Jurković *et al.*, 2012). Serpentine carbonation onsets by the dissolution of atmospheric CO_2 into water, where CO_2 forms different species as a function of pH. At pH < 6.5, carbonic acid (H_2CO_3) dominates, at pH between 6.5 and 10.5, bicarbonate (HCO_3^-) dominates and at higher pH, carbonate anion (CO_3^{2-}) dominates. Serpentine dissolution and magnesite precipitation are also pH-dependent (Klein and Langmuir, 1987; Guthrie *et al.*, 2001; Tneir *et al.*, 2007; Prigiobbe *et al.*, 2009; Teir *et al.*, 2009; Krevor and Lackner, 2011). Experimentally, Teir *et al.* (2007) have shown that the best efficiency for serpentine to carbonate conversion is obtained in the pH range of 8-11, with an optimum at pH 9. Roughly similar pH conditions were measured for the optimum carbonation of olivine (Prigiobbe *et al.*, 2009). At pH > 8, bicarbonate starts to dissociate into H^+ and CO_3^{2-} ions:

$$HCO_3^- \rightarrow H^+ + CO_3^{2-} \quad (1)$$

Interaction between CO_2-rich water and serpentine gives rise to the exchange of H^+ and Mg^{2+} cations on the mineral surface. This reaction produces silica and water, while free Mg^{2+} cations react with CO_3^{2-} anions to form magnesite:

$$Mg_3Si_2O_5(OH)_4 + 6H^+ \rightarrow 3Mg^{2+} + 2H_4SiO_4 + H_2O \quad (2)$$

$$Mg^{2+} + CO_3^{2-} \rightarrow MgCO_3 \quad (3)$$

The overall reaction can be summarized as follow:

$$Mg_3Si_2O_5(OH)_4 + 3(2H^+ + CO_3^{2-}) \rightarrow 3MgCO_3 + 2SiO_2 + 5H_2O \quad (4)$$

$$\text{Serpentine} + CO_{2(aq)} \rightarrow \text{Magnesite} + \text{Silica}_{(aq)} + \text{Water}$$

Worldwide, carbonation of serpentinite commonly leads to the formation of magnesite deposits in association with ophiolitic bodies, *e.g.* in California (Bodenlos, 1950; Sherlock and Logan, 1995), Egypt (Ghoneim *et al.*, 2003), Greece (Dabitzias, 1980), Italy (Cipolli *et al.*, 2004), Norway (Beinlich *et al.*, 2012) or Oman (Kelemen and Matter, 2008). In New Caledonia, similar magnesite deposits have been described in the serpentine sole of the ophiolite, but few studies have focused on the origin of this magnesite (Glasser, 1904; Trescases, 1973; Ulrich, 2010; Quesnel *et al.*, 2013). Quesnel *et al.* (2013) propose that magnesite veins in the serpentinite sole formed tectonically, at temperatures between 40 and 80°C. On the basis of stable isotope analyses (O and C), these authors propose that the fluid from which magnesite formed was originally meteoric water and that the carbon source is mostly atmospheric, with a possible biogenic contribution. They also suggest that magnesium originated from the dissolution of the peridotite at the top of the ophiolite during laterization and was transferred down to the sole by the infiltration of meteoric waters under tectonically active conditions. The *per descensum* model is largely invoked to explain magnesite deposits in lateritic environments (Dabitzias, 1980; Pefrov *et al.*, 1980; Pohl, 1990; Abu-Jaber and Kimberley, 1992a; 1992b; Foster *et al.*, 2002; Jurković *et al.*, 2012; Oskierski *et al.*, 2012). It requires a well-drained system where meteoric waters, charged with atmospheric CO_2, dissolve serpentine (and other Mg-silicates), a process that releases magnesium and silicon into solution. Meteoric waters then percolate downward thanks to a microfracturing permeability system, thus dissolving more magnesium. Within this frame, precipitation of magnesite is due to supersaturation of fluids, which are generated by the neutralization of carbonic acid by serpentine dissolution, as shown by reactions (2) and (3) (Bodenlos, 1950; Pohl, 1990; Fallick *et al.*, 1991; Abu-Jaber and Kimberley, 1992b; Giammar *et al.*, 2005; Kelemen *et al.*, 2011). Alternatively, the ultramafic pile may become a partially closed system, and therefore limit the exchange between atmospheric CO_2 and meteoric water (Jurković *et al.*, 2012). Progressive dissolution of serpentine during the fluid migration downwards consumes H^+ ions, as shown by reaction (3). As CO_2 is not freely available anymore, such consumption of H^+ ions causes the increase of pH, enhancing magnesite precipitation (Jurković *et al.*, 2012).

Considering the origin of magnesium as deriving from the laterization rises the question about the mechanism of magnesite precipitation in New Caledonia. In such a case, and similarly to magnesite deposits from Euboea (Greece, Boydell, 1921), magnesite formation may be the result of direct precipitation from the fluids without interacting with hosted rocks of the deposit site. This hypothesis was favored by the composition of New Caledonia waters passing through peridotites

and serpentinites (sampled in la Coulée river, Mont-Dore), showing that they are enriched in magnesium and CO_3^{2-} ions (Barnes *et al.*, 1978). Alternatively, field investigations highlight a close relationship between serpentinite, magnesite and silica, suggesting that the two latter phases may originate from the dissolution of the former. In this case, magnesite would precipitate by *in situ* replacement of the serpentine, using magnesium released during the serpentine dissolution. In this study we provide evidences of magnesite formation through such a process on the basis of mineral characterization using an original analytical method for the interpretation of micro-X-Ray Fluorescence (µ-XRF) images. We particularly focus on the formation process of magnesite veins coupled to intense silicification observed in the serpentinite sole of the New Caledonia ophiolite.

1. GEOLOGICAL SETTINGS AND SAMPLE DESCRIPTIONS

New Caledonia is located in the SW Pacific, 2000 km east of the Australian coasts (Figure 1). It is composed of several islands that belong to the Norfolk ridge (La Grande Terre, Island of Pines, Belep Islands) and to the Loyalty ridge (Loyalty Islands). The main island, la Grande Terre, consists of a patchwork of terranes reflecting the geodynamic evolution of the SW Pacific region from late Permien to Eocene (*e.g.* Cluzel and Meffre, 2002; Cluzel *et al.*, 2001; 2012). Among these terranes, the ophiolite is the most prominent as it covers more than 25% of the island. The so-called Peridotite Nappe is composed of a large and continuous massif located south of the island and some isolated klippes widespread along the west coast (Figure 1). The ophiolite was formed between 83 Ma with the opening of the South Loyalty Basin and its subsequent closing at 34 Ma, timing of its obduction on the Norfolk continental basement (Cluzel *et al.*, 2001; Crawford *et al.*, 2003; Schellart *et al.*, 2006; Whattam *et al.*, 2008; Whattam, 2009; Ulrich *et al.*, 2010; Cluzel *et al.*, 2012). Since its emergence, the uppermost part of the Peridotite Nappe has undergone an intense laterization. This led to the development of a thick laterite bed (up to 60 m thick; Sévin et al., 2012) that owns ~30% of the world nickel resources. The whole ophiolite is formed of upper mantle rocks (mainly harzburgites) with minor cumulates (Prinzofher, 1981). Peridotites are highly serpentinized, particularly at the base of the ophiolite which is made of a thick (up to 400 m thick, Audet, 2010; Ulrich *et al.*, 2010) and silicified serpentinite sole where large amount of magnesite veins have crystallized (Quesnel *et al.*, 2013).

Samples presented in this study were collected in the serpentinite sole of the Koniambo massif (Figure 1). Similar outcrops occur on the serpentinite sole from other peridotite massifs in

New Caledonia (Ulrich, 2010). In the field, the whole sole is highly deformed, finely schistose and/or intensely brecciated, and has recorded multiple serpentinization events (Ulrich, 2010): Massive serpentinization, which is of a typical bottle-green color in the field (Figure 2), is cross-cutted by light-green colored serpentine veins. The latter is associated with black magnetite impregnations and micro-cracks filled by fibrous serpentine (chrysotile). Magnesite occurs as millimeter to multi-decimeter stock-work veins with a typical cauliflower-like texture, cross-cutting serpentinites (Figure 2). The magnesite is mainly snow-white colored, but can also appear greenish depending of the amount of intergrown serpentine. On the basis of structural observations, Quesnel *et al.* (2013) distinguished two types of veins. The first type of veins is observed along and/or within the margins of top to the SW-centimeter shallow dipping shear zones. The second type of veins corresponds to steeper veins occasionally crosscut by the low-dipping shear zones. Magnesite can also develop pervasively by precipitating in large and massive serpentine blocks (Figure 2 a, b, c). In this case, the magnesite seems to develop first at the expense of the light-green colored serpentine to progressively extend to bottle-green serpentine, a relationship that is not clear when magnesite fills the main shear zones, as described by Quesnel *et al.* (2013).

2. ANALYTICAL METHODS

1. X-Ray Diffraction

Analyzes were performed at the Institut des Sciences de la Terre (ISTerre, Grenoble, France) on sample powders obtained after the crushing of separated magnesite veins and serpentinite host rock mineral fractions. X-ray diffraction (XRD) patterns were recorded with a Bruker D5000 powder diffractometer equipped with a Kevex Si(Li) solid state detector using $CuK\alpha_{1+2}$ radiation. Intensities were recorded at 0.02° 2θ step intervals from 5 to 80°, with a 6 seconds counting time per step. Size of the divergence slit was 0.298°.

2. Raman Spectroscopy

Raman spectroscopy measurements were performed at the Ecole Normale Superieure of Lyon and at GéoRessources Nancy, France, in both cases using a Horiba Jobin-Yvon LabRam HR800 spectrometer and a visible ionized argon laser source with a wavelength of 514 nm. Output laser power was 100 mW, and measurements were performed using an Olympus lens of x100 to focus the

laser beam onto an area that was 1 μm in diameter. Analyzes were done on macroscopic samples and on thin sections. Spectra result from the average of 5 acquisitions of 10 s to 20 s to optimize the signal/noise ratio. Two regions of the Raman spectra were investigated: 150-1250 cm^{-1} for structural bonding characterization and 2800-3900 cm^{-1} for the characterization of the hydroxyl groups.

3. Micro-X-ray Fluorescence

Micro-X-ray Fluorescence (μ-XRF) analyses were performed on a 5 mm-thick rock section (Figure 2d) using EDAX Eagle III spectrometer at ISTerre (Grenoble, France). The X-ray tube consists of a Rh anode operating at 250 μA with an acceleration voltage of 40 kV. Polycapillary lenses were used to focus the X-ray beam down to 40 μm full-width-at-half-maximum at the sample surface. An energy dispersive X-ray detector with resolution of 140 eV was used to measure fluorescence spectra. Chemical maps were recorded with a matrix of 256 x 200 pixels, a 40 μm step interval in both directions, and a dwell time of 1 s per pixel. For each map, the grey-scale corresponds to the intensity of the Kα-lines of the different elements (Si, Mg, Fe, Al, Ni, Ti, Mn, Cr, Ca, K) calculated from the integration of a specified region of interest (ROI) of the energy-range of XRF spectra. Then, ROI maps (see electronic supplements, Figure S4) are used to calculate phase maps thanks to a new routine, specially developed Matlab©-based code, following the same approach than that successfully applied first to the computing of mineral-phase maps from hyperspectral μ-XANES mapping (Muñoz *et al.*, 2008). In the case of hyperspectral μ-XRF maps, the phase map calculation consists first of determining pure mineral phases that are expected to be present in the sample, in order to create standard spectra (or "pure" spectra). Then for each pixel of the map, a linear combination of the different standard spectra is performed in order to fit each single spectrum. Results provide quantitative phase maps showing the distribution of minerals previously identified in the sample (*e.g.*, based on XRD and/or Raman analyses). This approach is particularly useful to highlight relationships between minerals, especially for the characterization of finely-divided mineral assemblages, *i.e.* when the beam is larger than grain size (such as here, typically below 1 micron). Concentration maps (in wt.%) are finally recalculated on the basis of phase distribution maps considering the chemical composition of standards (Table 1)

4. RESULTS

1. Mineralogy and chemical compositions

a. Bulk mineralogical compositions

Figure 3 shows the X-ray diffraction patterns obtained on separated fractions of serpentinite and magnesite. The serpentinite mainly consists of serpentine with minor amount of magnetite and chromite. Serpentine occurs as lizardite and chrysotile. The occurrence of chrysotile is consistent with the presence of fibrous serpentine in microcracks as described above. Despite a careful separation, small peaks of magnesite and silica are present in the diffraction pattern of the serpentinite, suggesting that both minerals also occur at the micrometer scale within the hosted rock.

XRD pattern of magnesite powder shows that the carbonate exhibits its most characteristic reflections at the following *d* values (in Å, arranged according to decreasing intensities): 2.74, 2.10, 1.70, 2.50, and 1.94 (Figure 3). In addition, the diffraction pattern shows that magnesite systematically integrates small amounts of sepiolite ($Mg_4Si_6O_{15}(OH)_2•6(H_2O)$), a mineral that is frequently described in association with carbonate in ultramafic environments (*e.g.* Birsoy, 2002*;* Yaliçin and Bozkaya, 2004; Boschetti and Toscani, 2008). On the basis on this XRD pattern, magnesite is the only carbonate to crystallize. Neither dolomite nor calcite are formed, contrarily to numerous magnesite deposits previously described in the literature (Griffis, 1972; Dabitzias, 1980; Jedrysek and Halas, 1990; Fallick *et al.*, 1991; Abu-Jaber and Kimberley, 1992b; Lugli *et al.*, 2000; Zedef *et al.*, 2000; Ghoneim *et al.*, 2003; Jurković *et al.*, 2012).

b. Optical microscopy

Figure 4 shows the typical mineralogical textures of carbonated serpentinites composing the sole of the New Caledonia ophiolite. In thin section, the serpentinite does not exhibit any relic of primary minerals (*i.e.* olivine and pyroxene). However, the habits of grains and original textures of primary minerals (*e.g.* cleavage planes of orthopyroxene) have been preserved (typical pseudomorphic “mesh” texture, Figure 4a, b) and indicate that the parent rock was a harzburgite. As highlighted by XRD analyzes, opaque minerals associated with the serpentine are small grains of magnetite and chromite disseminated in the mesh. In these rocks, magnesite occurs as finely disseminate grains (*i.e.* cryptocrystalline texture) that developed both at the rim and in cracks affecting serpentine grains (Figure 4b, d). These grains progressively aggregate to form larger zones with a typical granular texture (Figure 4a-c). The sepiolite, identified by XRD and optical microscopy, occurs as brown fibers interstitially to the magnesite nodules (Figure 4c). Silica also occurs close to magnesite. Microscopic observations show that the nature of the silica is variable: it

occurs as an amorphous solid (gel-like) surrounding magnesite aggregates and serpentine grains in area where magnesite dominates (Figure 4a, c, d). Where serpentine is dominant, silica consists of crystalline to fine grains, forming vugs with a typical colloform texture propagating in the serpentine mesh (Figure 4e, f). In this case, the nature of silica ranges from amorphous-like near the rim of the vug to quartz-like at the center (Figure 4c, e, f).

c. Raman spectroscopy

Raman analyses were performed to further identify minerals that compose the serpentinite. This technique is complementary to XRD, since it is particularly efficient to distinguish among the different varieties of serpentine (*e.g.* Lemaire, 2000; Auzende *et al.*, 2004) as well as silica polymorphs (*e.g.* Götze *et al.*, 1998; Pop *et al.*, 2004). Figure 5 shows Raman spectra collected on carbonated serpentinites. Results show that lizardite is the dominant serpentine variety that occurs as individual grains and in the mesh, and corresponds to the bottle-green colored serpentine described in the macroscopic observations. Chrysotile (not shown in Figure 5) has also been detected, as already highlighted by XRD. In addition, light green serpentine was identified as polygonal serpentine. It shows quite similar patterns to those of the lizardite at low wavenumbers, but strongly differs at high wavenumbers (from 3500 to 3800 cm^{-1}, corresponding to OH group), where the polygonal serpentine is characterized by a large peak composed by two bands centered at 3689 and 3700 cm^{-1} (*e.g.* Lemaire, 2000; Auzende *et al.*, 2004).

The Raman spectrum of magnesite is characterized by four distinct bands located at 209, 327, 737 and 1094 cm^{-1} (Figure 5), consistently with the work of Krishnamurti (1956). The lack of bands at 3448 and 3648 cm^{-1} (*i.e.*, in the OH region; typical of hydromagnesite) shows that magnesite is anhydrous.

Silica polymorphs are clearly identified using Raman spectroscopy. Vug rims consist of opal-CT (Silica #1, Figure 4e) while brown coronas (Silica #2, Figure 4e) and white fine grains (Silica #3, Figure 4e) inside of the vugs are identified as chalcedony (Figure 5). Although significantly different in microscopic observations (Figure 4e, f), both chalcedonies display very similar Raman spectra, except on the intensity of the band located at 501 cm^{-1} which is significantly higher in the white chalcedony (electronic supplements, Figure S1). Notice that in all silica polymorphs, the large bands observed between 3100 and 3900 cm^{-1} indicate the presence of molecular water.

d. XRF mapping

The elemental distribution, expressed in weight percent, in a typical serpentinite texture surrounded by magnesite is shown in Figure 6. On the basis of chemical measurements, it was not possible to discriminate lizardite from polygonal serpentine, both having very similar compositions. Therefore, we only refer to serpentine in the followings, focusing on the nature of processes that preferentially affect the serpentine grains or the mesh. The distribution maps of MgO and SiO_2 highlight serpentine grains (s) as well as mesh texture (m). The chemical composition of these grains is consistent with the stoichiometry of serpentine minerals, with about 43 wt.% for both MgO $+Fe_2O_3$ and SiO_2. However, SiO_2 concentration in the mesh is significantly higher, and can reach up to 65 wt.%. To better understand such differences in chemical compositions, we calculated the phase distribution maps according to the minerals that are expected to be present in this sample (Figure 7 and electronic supplements, Figure S4). Phase distribution reveals that the central zone of the mapped area mainly consists of serpentine minerals. The amount of serpentine is at least 50 % in the mesh and close to 100 % in grains. Silica distribution is relatively homogeneous in the mesh, with about 30 % silica, but shows peculiarities close to the magnesite, where the silica content reaches about 100 %. In contrast, the amount of silica in serpentine grains is well below 5 %. Finally, the calculation of phase distribution maps was obtained with about 20 % of magnesite in the serpentinite texture (*i.e.* the central area).

Figure 8 shows density correlation diagrams between serpentine, magnesite and silica based on the phase distribution maps for the two regions delimited by squares in Figure 7. These diagrams statistically illustrate the description made above on the phase maps and reveal two distinct processes. In the region 1, the diagrams show a clear anticorrelation between silica and serpentine, corroborating that a great part of the pixels of this region corresponds to "silicified serpentine". At the opposite, the relationships between magnesite and serpentine on one hand and those between silica and magnesite on the other hand are less straightforward. To better understand these two diagrams, the region 2 (dashed square in Figure 7) was delimited around a heterogeneous serpentine grain that appears partially altered (Figure 9). This alteration occurs around fractures in the grain and is expressed by a lighter color of the serpentine in microscopic view. Considering this grain, a statistical analysis shows that silica and magnesite are correlated to each other, whereas they are both anticorrelated to serpentine (Figure 8, region 2). This point is particularly interesting since the phase maps clearly highlight here a process of replacement of serpentine by an assemblage of magnesite and silica. Even if silica and serpentine are anticorrelated in both regions, carbonation and silicification processes do not follow rigorously the same trend. On the basis of our specific treatment of the XRF maps, we demonstrate here that the serpentinite is affected by two distinct

weathering processes: while the mesh texture is mainly affected by a silicification process, the serpentine grains are mainly affected by the crystallization of a magnesite + amorphous silica assemblage.

5. DISCUSSION

Serpentinite carbonation in New Caledonia has a supergene origin, following a *per descensum* model (Glasser, 1904; Trescases, 1973; Ulrich, 2010; Quesnel *et al.*, 2013). The atmospheric carbon dioxide is first dissolved in meteoric water. The CO_2-enriched fluids then circulate through the lateritic cover, dissolve the residual Mg-rich minerals before driving to the precipitation of magnesite in fractures and to a porosity reduction in the serpentinite, within the serpentinite sole. This carbonation process leads to the formation of clusters of magnesite, potentially very large, and usually very localized to the serpentine rich fractures or volumes. Although this process is most easily observed in the field, our results show that the serpentine dissolution leads to the local crystallization of magnesite and silica. This diffuse process is potentially the main mechanism of carbonation of the serpentinite sole.

1. Carbonation after serpentine dissolution

On the basis of our results of our mineralogical investigations, several features provide evidence that magnesite precipitation occurs through serpentine dissolution. First, the development of magnesite along the edges of adjacent serpentine grains is a characteristic of carbonation by *in situ* replacement of the serpentine (Figures 4b, 4d and 9). When serpentine grains are preserved, carbonation is limited to the rims, the core remaining unaffected. At the opposite, the dissolution and replacement of the serpentine are more efficient in case of fractured grains (Figure 9). This observation is consistent with experimental studies showing that intense grain fracturing is required to ensure complete carbonation (*e.g.* Haug *et al.*, 2011; Kelemen *et al.*, 2011; Hövelmann *et al.*, 2012; van Noort *et al.*, 2013). Another way to illustrate the progressive serpentine carbonation is given by Figure S2 (in electronic supplements). Here, the RGB map (for Red, Green, Blue, see the figure caption for more details) shows that magnesite is ubiquitous, formed by the replacement of the serpentine grains, and that only a few of the latter are preserved from the carbonation process. In addition, considering the stoichiometry and the molar volumes of the mineral species involved in reaction (4), volumes of magnesite and silica produced by the dissolution of 1 mole of serpentine

(108 cm^3) are respectively 85 cm^3 and 58 cm^3 (V_{Mgs}/V_{Silica} ~1.45), leading to a volume increase of about 30 %. Statistics calculated on the serpentine grain presented in Figure 9 (corresponding to the region 2, Figure 7) show that the assemblage consists of about 62 vol.% of serpentine, 21 vol.% of magnesite and 15 vol.% of silica (V_{Mgs}/V_{Silica} ~1.4; Figure 8). This assemblage compares well with the result of dissolution of 38 vol.% of serpentine, which leads to the formation of ~22 vol.% of magnesite and ~15 vol.% of silica. These estimates testify that results given in the phase maps are in good agreement with the stoichiometry of reaction (4). Second, carbonation by serpentine dissolution is also evidenced by the precipitation of an amorphous silica layer at the grain rims (Figure 4d). This observation is consistent with the previous studies that systematically reported the formation of a Si-rich layer after Mg-bearing mineral breakdown (*e.g.* Luce *et al.*, 1972; Lin and Clemency, 1981; Guthrie *et al.*, 2001; Schulze *et al.*, 2004; Giammar *et al.*, 2005; Bearat *et al.*, 2006; Sipilä *et al.*, 2008; Andreani *et al.,* 2009; Daval *et al.,* 2011*;* King *et al.*, 2011, Hövelmann *et al.*, 2011; 2012). Third, sepiolite, which is described in our samples in association with magnesite (Figures 3 and 4c), also formed subsequently to the dissolution of serpentine (*e.g.* Jones and Galàn, 1988; Birsoy, 2002; Yaliçin and Bozkaya, 2004; Andreani *et al.*, 2009). Similar occurrences of sepiolite have been reported during natural (Yaliçin and Bozkaya, 2004) and experimental (Andreani *et al.*, 2009) carbonation of Mg-bearing minerals (serpentine and olivine). Actually, sepiolite may form in different ways:

$$2Mg_3Si_2O_5(OH)_4 + 2(2H^+ + CO_3^{2-}) + 2H_4SiO_4 \rightarrow 2MgCO_3 + Mg_4Si_6O_{15}(OH)_2.6H_2O + 3H_2O \quad (5)$$

$$\text{Serpentine} + CO_{2(aq)} + \text{Silica}_{(aq)} \rightarrow \text{Magnesite} + \text{Sepiolite} + \text{Water}$$

$$3Mg_3Si_2O_5(OH)_4 + 5(2H^+ + CO_3^{2-}) \rightarrow 5MgCO_3 + Mg_4Si_6O_{15}(OH)_2.6H_2O + 4H_2O \quad (6)$$

$$\text{Serpentine} + CO_{2(aq)} \rightarrow \text{Magnesite} + \text{Sepiolite} + \text{Water}$$

$$Mg_3Si_2O_5(OH)_4 + 2.5(2H^+ + CO_3^{2-}) \rightarrow 2.5MgCO_3 + 0.125Mg_4Si_6O_{15}(OH)_2.6H_2O + 1.25H_4SiO_4 + 1.125H_2O \quad (7)$$

$$\text{Serpentine} + CO_{2(aq)} \rightarrow \text{Magnesite} + \text{Sepiolite} + \text{Silica}_{(aq)} + \text{Water}$$

All these reactions contribute to form magnesite, but they differ as reactions (5) and (6) conserve all Mg and Si in solids and are characterized by a volume gain (~60% and ~30%, respectively) while reaction (7) is balanced on volume. In addition, Eq. (5) consumes silica while Eq. (7) produces it. Only on the basis of cm-scale maps, it is difficult to estimate which reaction occured: in our sample, sepiolite represents less than 1 vol.% (see electronic supplements, Figure S4). Among the reactions

written above, Eq. (7) is the one that produces the smallest amount of sepiolite, regarding the amount of magnesite that stoichiometrically precipitates. In contrast, Birsoy (2002) demonstrated that sepiolite formation is much more favored in the presence of Si-rich solution. In that case, sepiolite in our sample may derive from Eq. (5).

The fact that some serpentine grains are only partially transformed into magnesite indicates that the carbonation process was not completed. The reason why the reaction does not go to completion may be due to (1) silica precipitation, (2) pH increase and/or (3) porosity decrease. Numerous studies proposed that the formation of a Si-rich layer at the rims of serpentine grain during the first steps of dissolution might inhibit further Mg diffusion, potentially retarding or even stopping the process of carbonation (Gerdemann *et al.*, 2003; Schulze *et al.*, 2004; Alexander *et al.*, 2007; Daval *et al.*, 2011). Although Si-rich layer effectively reduces the accessibility of fluids to the reactive surface of minerals, recent investigations demonstrate that some permeability is maintained as carbonation remains active even after its development (Béarat *et al.*, 2006; Andreani *et al.*, 2009; Hövelmann *et al.*, 2012). Thus, it is not obvious that precipitation of Si-rich layer led the serpentine carbonation to stop. Alternatively, following reaction (4), the dissolution of serpentine consumes 2 moles of H^+ for 1 mole of CO_3^{2-}, leading to a progressive increase of fluid pH. According to Barnes *et al.* (1978), fluids reacting with serpentinite in New Caledonia have pH ranging from 9 to 11. At pH 9, HCO_3^- dominates over CO_3^{2-}, making the serpentine dissolution possible following reactions (1) and (2). At pH 10.5, CO_3^{2-} species become dominant and at pH 10.8, HCO_3^- represent less than 20% of the carbonate species in the fluid. In these conditions, magnesite precipitation is favored, but serpentine dissolution is scarce due to the lack of H^+ ions (*e.g.* Teir *et al.*, 2007). Thus, intensive exchange between H^+ ions and Mg^{2+} cations on the serpentine surface leads to a progressive increase of pH that may inhibit further serpentine dissolution and subsequent carbonation. There is no evidence to argue against such process in New Caledonia, but it requires that atmospheric CO_2 is not freely available and thus a roughly closed system (Jurković *et al.*, 2012). A third explanation may account for the inhibition of carbonation. Hövelmann *et al.* (2012) recently investigated the microstructure and porosity evolution as a function of carbonation reaction progress in natural peridotite. On the basis of their experimental results, they reported that a carbonation extend of ~10 % leads to a closure of 50 % of the initial porosity. They demonstrated that magnesite precipitation in fracture pore space reduces the permeability and progressively stops the fluid pathway, preventing further reaction between the fluid and the silicate surface and ultimately ends the carbonation process. Contrarily to serpentinization, which is able to propagate through a reaction-

induced fracturing mechanism (*e.g.* Plümper *et al.,* 2012), carbonation is self-limited as the reaction will be inhibited due to magnesite growing that ultimately clogs the system. This implies that no volume gain occurs at the rock-scale (Beinlich *et al.*, 2012). Numerous studies highlight the necessity of active fracturing to ensure complete carbonation (*e.g.*, Kelemen and Matter, 2008; Kelemen *et al.,* 2011; Boschi *et al.*, 2012). In our samples, no evidence of carbonation-induced fracturing has been observed so far, even if Quesnel *et al.* (2013) show the syn-kinematic character of magnesite veins at the outcrop scale. At the millimetric scale, volume gain associated with reaction (4) may have inhibited the complete carbonation of serpentinite by clogging the reacting zone. Such a process may prevent the infiltration of additional fluids, resulting in the partial carbonation of serpentine grains as illustrated by Figure 7 (see also electronic supplements, Figure S2).

2. Redox conditions during magnesite precipitation

The behavior of iron during carbonation has been poorly investigated. Such information would be indicative of redox conditions during magnesite precipitation. In serpentinite, iron is mainly hosted by iron oxides (magnetite, Fe_3O_4) surrounding serpentine grains or disseminated in the mesh texture (see electronic supplement, Figure S5). Iron content in serpentine is ~2 wt.% (expressed as FeO, Table 1). It substitutes Mg^{2+} cations in octahedral sites (O'Hanley, 1996). During serpentine dissolution, iron is released from the mineral structure and may subsequently form Fe-Si-rich layer that progressively evolves into magnetite at the interface between serpentine and aqueous fluid (Fallick *et al.*, 1991; Alexander *et al.*, 2007; Andreani *et al.*, 2009, Saldi *et al.*, 2013). Alternatively, it may precipitate as siderite ($FeCO_3$) under rather high pCO_2 and specific pH range from 5.5 to 7.5 (Ohmoto *et al.*, 2004) or be integrated in magnesite by substituting Mg^{2+} cations (Abu-Jaber and Kimberley, 1992b; Hansen *et al.*, 2005). In each of these minerals, iron oxidation is expected to differ according to oxidizing conditions: it is mostly oxidized in magnetite (*i.e.* 2/3 of iron is ferric iron) while it is in ferrous state in siderite or magnesite. In our sample, XRF analyzes show that the iron content in magnesite is very low (Table 1), suggesting that its integration into the structure of the magnesite was very scarce. In addition, we never identified siderite in our samples so far. As stated above, siderite precipitates at pH conditions that are significantly lower than those of New Caledonia waters, so it is likely that pH was too high to make siderite precipitate. Magnetite is ubiquitous in our sample. Therefore, discriminating magnetite grains related to prior serpentinization events to those potentially derived from carbonation is not obvious. However,

microscopic observations show that numerous magnetite grains have precipitated inside of partially carbonated serpentine grains (Figures 4d and 9) while magnetite related to serpentinization generally forms outside of serpentine grains. Schematic representation in Figure 9 highlights the systematic association of magnetite with cracks in the serpentine grain. According to Andreani *et al.* (2009), such grain fracturing may be considered as zones of localized fluid flow that favor the precipitation of magnetite during the first step of mineral dissolution. In contrast, their experiments show that carbonation initiates in domains of reduced fluid flow zones (fractures of a smaller size) where chemical gradient are small and thus facilitate local supersaturation, high pH and more reducing conditions. These results indicate that magnetite associated with the carbonation process may be used as a proxy to estimate the fluid flow rate at the serpentine grain scale: Fractures filled by magnetite correspond to high fluid flow zones characterized by more oxidizing conditions. In these regions, dissolution occurs but not magnesite precipitation (Andréani *et* al., 2009). Magnesium migrates to zones of reduced fluid flow, corresponding to regions dominated by magnesite or partially carbonated serpentine (Figures 9. 10). In these areas magnesite precipitates due to local supersaturation under more reducing conditions. This underlies that redox gradients occur even at grain scale.

3. Serpentine mesh silicification

a. Silica mobilization and precipitation

Intense silicification of the serpentine mesh was revealed during this study based on XRF measurements and Raman spectroscopy (Figures 6-8, electronic supplements, Figures S2 and S3). For instance, the region 1 (Figure 7) is composed of 62 vol.% of serpentine, 24 vol.% of silica and 7 vol.% of magnesite in average. The precipitation of 7 vol.% of magnesite consumes 12 vol.% of serpentine and forms 5 vol.% of silica, on the basis of reaction (4). Such excess of silica necessarily involves a contribution of silica from outside of the region 1. Phase maps show that pure silica mainly occurs in gaps between magnesite aggregates (left-side of the map, Figure 7 and electronic supplements, Figure S2). However, when aggregates agglomerate subsequently to magnesite growth (right-side of the map, Figure 7 and electronic supplements, Figure S2), silica is expelled from the magnesite. Numerous experimental studies indicate the progressive migration of silica rather than being rejected from the growing magnesite (Schulze *et al.*, 2004; Hövelmann *et al.*, 2011; 2012). As stated above, the first steps of serpentine dissolution release silica that immediately precipitates as a Si-rich layer. As carbonation reaction proceeds, the released silicon may feed the

growth of the Si-rich layer, but Hövelmann *et al.* (2012) reported that such inward growth is limited. This limitation is mainly associated with pH increase of fluid during the carbonation process. At pH>9, magnesite precipitates while silica is solubilized and is therefore able to migrate away from the solid-fluid interface. Occurrence of water within silica is demonstrated by the Raman spectrum measured in the region of high frequencies (Figure 5), which exhibits a typical spectrum of molecular water. As illustrated by XRF mapping, fluids enriched in silica subsequently to serpentine dissolution, propagates in the serpentine meshwork. Similar observations have been reported in serpentinites from the Oman and the Ligurian ophiolites (Stanger, 1985; Boschi *et al.,* 2009; Lacinska and Styles, 2012). According to Lacinska and Styles (2012), the well-preserved mesh texture (as observed in our samples) induces a combination of iso-volumetric processes of slow rate dissolution of the mesh serpentine and immediate local precipitation of silica. They also argue that precipitation of silica is favored at near-neutral pH conditions. Such conditions differ from those we assume in our system (high alkali pH). However, Williams and Crerar (1985) attributed the precipitation of amorphous silica phases in nature due to the formation of dense colloids in supersaturate alkaline aqueous solutions. In addition, progressive dissolution of silica causes pH of the solution to drop (Williams and Crerar, 1985; Williams *et al.*, 1985). Following these observations, we infer that such process may favor the dissolution of the serpentine mesh and the subsequent grain-by-grain replacement by amorphous silica phases, as postulated by Lacinska and Styles (2012). Such a process involves the removal of substantial amount of magnesium. As shown above, serpentine grain carbonation occurs stoichiometrically, *i.e.* magnesium released after serpentine grain dissolution, then immediately precipitates as magnesite. Thus, it is likely that the magnesium released during serpentine mesh silicification migrates out of the reaction zone. This assumption is consistent with the study of Boschi *et al.* (2009) that reported similar magnesium mobilization after serpentine dissolution and silica precipitation.

b. Silica evolution

Raman spectroscopy shows that silica formed in response to serpentine carbonation crystallizes as opal-CT and chalcedony (Figure 5). Such silica polymorphs are commonly described in association with magnesite and are consistent with formation at low temperature conditions (Boydell, 1921; Bodenlos, 1950; Dabitzias, 1980; Pohl, 1990; Abu-Jaber and Kimberley, 1992b; Klein and Garrido, 2011). According to Lacinska and Styles (2012), the formation of opal-CT indicates precipitation from supersaturated fluids. Williams *et al.* (1985) and Williams and Crerar (1985) show that the precipitation of silica polymorphs is driven by multiple steps of dissolution-

precipitation. Systematically, studies made on the silica diagenesis report that saturated silica solutions do not form opal-CT directly, but follow a sequential crystallization with first the precipitation of amorphous opal-A (Graetsch *et al.*, 1985; Williams *et al.*, 1985; Williams and Crerar, 1985; Heaney, 1993; Lacinska and Styles, 2012). Opal-A then evolves by means of dissolution–precipitation with concurrent ordering of the structure and removal of water, forming a pathway as follow: opal-A (amorphous) ⟶ opal-CT (cristobalite-tridymite assemblage)⟶ chalcedony ⟶ quartz. According to Williams *et al.* (1985), the relationship between solubility and surface area or particle size is sufficient to explain such evolution. In our samples, only opal-CT and chalcedony have been identified so far. One possible explanation to account for the absence of opal-A is the complete replacement by opal-CT. The association with magnesite supports this hypothesis, since carbonates are thought to enhance the formation of opal-CT (Williams and Crerar, 1985). Quartz has never been described associated with serpentinite in New Caledonia, so it is likely that the transition chalcedony to quartz does not occur. This reaction is very slow and is more likely to occur in a closed system, from the precipitation of fluids undersaturated in silica with respect to opal-A, opal-CT or chalcedony (Lund, 1960 and references therein; Williams *et al.*, 1985; Williams and Crerar, 1985). In our samples, vugs containing chalcedony are systematically characterized by the presence of a hole on its center (Figure 4). Similar observations were reported by Lund (1960) from silicified corals where both chalcedony and quartz precipitated. This author concluded that the hole served as a conduit for the continuous circulation of dissolved silica, resulting in the precipitation of chalcedony. At the opposite, when no hole was observed, chalcedony was completely replaced by quartz.

As an example, the concurrent reordering that occurs during the diagenetic pathway of silica is illustrated by the behavior of chalcedony (Figures 4 and electronic supplement, Figure S1). Chalcedony, as many of the microcrystalline SiO_2 varieties, consists of an intimately intergrowth of α-quartz and moganite. Moganite is a silica polymorph that typically contains up to 3 wt.% of water which is not a constituent of the structure. Using Raman spectroscopy, Pop *et al.* (2004) showed that during the opal-CT to chalcedony transition, moganite starts growing after α-quartz and preferentially in the most crystallized areas. It can be used as a proxy to evaluate the ordering of the chalcedony during its transition from opal CT to quartz (Götze *et al.*, 1998; Rodgers and Cressey, 2001; Pop *et al.*, 2004). In Figure 4c, both silica #2 and silica #3 have been identified as chalcedony but differ in microscopic observation by their colors. In Raman spectroscopy, silica #2 and silica #3 almost display the same patterns, except the intensity of the band at 501 cm^{-1} (moganite) that is higher in the white chalcedony (electronic supplement, Figure S1). The moganite content (in wt.%)

of chalcedony can be calculated using the Raman band integral ratios $I_{(501)}/I_{(465)}$ (*i.e.* moganite/ quartz) and applying the calibration curve proposed by Götze *et al.* (1998). We find that both chalcedonies are dominated by moganite, which represents 77 wt.% in brown chalcedony (silica #2, Figure 4c) and 81 wt.% in white chalcedony. The enrichment of moganite traduces the progressive ordering of chalcedony which ultimately transforms in quartz given sufficient time (Williams and Crerar, 1985; Heaney and Post, 1992; Rodgers and Cressey, 2001; Lynne *et al.*, 2007).

4. Coupled carbonation-silicification in dissolution-precipitation processes: a summary

Based on our results and those from previous experimental studies, we infer that serpentine carbonation occurred due to the circulation of high pH meteoric waters dissolving the serpentine. Serpentine dissolution started at grain boundaries and in large grain fractures that correspond to regions where the fluid flow is the highest (Figure 10a). In these regions, intensive exchanges between H^+ and Mg^{2+} ions led to the development of a Si-rich layer and the precipitation of magnetite at the mineral/water interface (Figure 10b). In contrast, magnesite precipitation was not favored in these zones of high fluid flow, which are characterized by strong chemical gradients and local oxidizing conditions (Andreani *et al.*, 2009). Released magnesium therefore migrated to regions of reduced fluid flow, where magnesite nucleated at the expense of serpentine surfaces by a process of dissolution-precipitation due to local supersaturation and more reducing conditions (Figure 10b-c). Here, the growth of magnesite was mainly fed by magnesium coming from the dissolution of adjacent serpentine grain. Potentially, distal contributions may have occurred (i.e. coming from the laterization, Barnes *et al.*, 1978), since magnesite incorporate calcium while this element is not concentrated in serpentine (Table 1). Silica released during the carbonation process may first have precipitated *in situ* as amorphous silica (opal A/CT), but progressive pH increase during the reaction facilitates the silicon solubilization and subsequent migration away from the fluid-solid interface (Figure 13c; Schulze *et al.*, 2004; Andreani *et al.*, 2009; Hövelmann *et al.*, 2011; 2012). Silica was then able to propagate in the serpentine mesh, silicifying the latter by precipitating first as an amorphous gel that progressively orders its crystalline structure to ultimately evolve as quartz if given sufficient time (Figure 10c; Williams and Crerar, 1985; Heaney and Post, 1992; Rodgers and Cressey, 2001; Lynne *et al.*, 2007). Magnesium leached during the serpentine mesh carbonation migrated out from its original reacting zone and potentially fed larger magnesite deposits in syn-tectonic fractures, as previously proposed by Boschi *et al.* (2009) in the Ligurian ophiolite. Carbonation process ended when the overall serpentine was converted into an

assemblage of magnesite + silica or, alternatively, when magnesite precipitation induced closure of the initial porosity (Figure 10d, Hövelmann *et al.*, 2012).

In agreement with recent studies from Andreani *et al.* (2009), Boschi *et al.* (2009), or Hövelmann *et al.* (2011; 2012), our study demonstrates the importance of active fracturing in the idea of *in situ* CO_2 sequestration. Although the volume extend expected during serpentine carbonation may lead to the system clogging, serpentine mesh silicification involves substantial removal of magnesium. This magnesium may migrate out of the reaction zone and subsequently precipitates as massive magnesite veins along the main structural discontinuities such as those described in New Caledonia by Quesnel *et al.* (2013). As previously underlined by Boschi *et* al. (2009), such a process may be considered as an alternative, efficient way for CO_2 sequestration.

Acknowledgements

The authors gratefully thank Gilles Montagnac (ENS Lyon) and Marie-Camille Caumon (GeoRessources Nancy) for their help during Raman analyses. We also thank Valerie Magnin (ISTerre Grenoble) for her help during μ-XRF analyzes and Clément Marcaillou (Eramet-SLN) and Olivier Vidal (ISTerre Grenoble) for their contributions on the development of the XRF-mapping software. This work has been possible thanks to the technical assistance of Koniambo SA, and benefited from the support of Labex Ressources 21 (Nancy). We thank the editor Jochen Hoefs and the two anonymous reviewers for their careful revisions that helped to improve this manuscript.

References

Abu-Jaber, N. S., and Kimberley, M. M. (1992a), Origin of ultramafic-hosted magnesite on Margarita Island, Venezuela, *Mineralium Deposita*, *27*(3), 234–241.

Abu-Jaber, N., and Kimberley, M. (1992b), Origin of ultramafic-hosted vein magnesite deposits, *Ore Geology Reviews*, *7*(3), 155–191.

Alexander, G., Mercedes Maroto-Valer, M., and Gafarova-Aksoy, P. (2007), Evaluation of reaction variables in the dissolution of serpentine for mineral carbonation, *Fuel*, *86*(1-2), 273–281.

Andreani, M., Luquot, L., Gouze, P., Godard, M., Hoise, E., and Gibert, B. (2009), Experimental study of carbon sequestration reactions controlled by the percolation of CO2-rich brine through peridotites, *Environmental Science & Technology*, *43*(4), 1226–1231.

Audet, M.A. (2008), Caractérisation pétrographique et structurale des matériaux ophiolitiques du massif de Koniambo (Nouvelle Calédonie) et des minéralisations nickélifères supergènes, Unpubished Thesis, Université du Québec à Montréal et Université de la Nouvelle-Calédonie, 355 pp.

Auzende, A., Daniel, I., Reynard, B., Lemaire, C., and Guyot, F. (2004), High-pressure behaviour of serpentine minerals: a Raman spectroscopic study, *Physics and Chemistry of Minerals*, *31*(5), 269–277.

Balucan, R.D., Dlugogorski, B.Z., (2013). Thermal Activation of Antigorite for Mineralization of CO_2, *Environmental Science & Technology*, *47*, 182–190.

Bain, G. W. (1924), Types of magnesite deposits and their origin, *Economic Geology*, *19*(5), 412–433.

Barnes, I., O'Neil, J., and Trescases, J. (1978), Present day serpentinization in New Caledonia, Oman and Yugoslavia, *Geochimica et Cosmochimica Acta*, *42*, 144–145.

Béarat, H., McKelvy, M. J., Chizmeshya, A. V., Gormley, D., Nunez, R., Carpenter, R. W., Squires, K., and Wolf, G. H. (2006), Carbon sequestration via aqueous olivine mineral carbonation: Role of passivating layer formation, *Environmental Science & Technology*, *40*(15), 4802–4808.

Beinlich, A., Austrheim, H. (2012). *In situ* sequestration of atmospheric CO_2 at low temperature and surface cracking of serpentinized peridotite in mine shafts, *Chemical Geology*, 332-333, 32–44.

Beinlich, A., Plümper, O., Hövelmann, J., Austrheim, H., Jamtveit, B. (2012). Massive serpentinite carbonation at Linnajavri, N-Norway, *Terra Nova,* 24, 446–455.

Birsoy, R., 2002. Formation of sepiolite-palygorskite and related minerals from solution. *Clays and Clay Minerals, 50(6)*, 736–745.

Bobicki, E.R., Liu, Q., Xu, Z., Zeng, H. (2012). Carbon capture and storage using alkaline industrial wastes, *Progress in Energy and Combustion Science, 38*, 302–320.

Bodenlos, A. (1950), Geology of the Red Mountain magnesite district, Santa Clara and Stanislaus Counties, California, *California Journal of Mines and Geology*, *46*, 223–278.

Boschetti, T., and Toscani, L. (2008), Springs and streams of the Taro–Ceno Valleys (Northern Apennine, Italy): Reaction path modeling of waters interacting with serpentinized ultramafic rocks, *Chemical Geology*, *257*(1-2), 76–91.

Boydell, H. C. (1921), The magnesite deposits of Euboea, Greece, *Economic Geology*, *16*(8), 507–523.

Cipolli, F., Gambardella, B., Marini, L., Ottonello, G., and Vetuschi Zuccolini, M. (2004), Geochemistry of high-pH waters from serpentinites of the Gruppo di Voltri (Genova, Italy) and reaction path modeling of CO2 sequestration in serpentinite aquifers, *Applied Geochemistry*, *19*(5), 787–802.

Cluzel, D., Aitchison, J., and Picard, C. (2001), Tectonic accretion and underplating of mafic terranes in the Late Eocene intraoceanic fore-arc of New Caledonia (Southwest Pacific): geodynamic implications, *Tectonophysics*, *340*(1-2), 23–59.

Cluzel, D., Meffre, S., (2002). L'unité de la Boghen (Nouvelle-Calédonie, Pacifique sud-ouest): un complexe d'accrétion jurassique. Données radiochronologiques préliminaires U-Pb sur les zircons détritiques, *Comptes Rendus Geosciences, 334*, 867–874.

Cluzel, D., Maurizot, P., and Collot, J. (2012), An outline of the Geology of New Caledonia; from Permian-Mesozoic Southeast Gondwanaland active margin to Cenozoic obduction and supergene evolution, *Episodes*, *35*(1), 72–86.

Crawford, A., Meffre, S., and Symonds, P. (2003), 120 to 0 Ma tectonic evolution of the southwest Pacific and analogous geological evolution of the 600 to 220 Ma Tasman Fold Belt System, vol. 22, pp. 377–397, Geological Society of Australia Special Publication.

Dabitzias, S. (1980), Petrology and genesis of the Vavdos cryptocrystalline magnesite deposits, Chalkidiki Peninsula, northern Greece, *Economic Geology*, *75*(8), 1138–1151.

Daval, D., Sissmann, O., Menguy, N., Saldi, G.D., Guyot, F., Martinez, I., Corvisier, J., Garcia, B., Machouk, I., Knauss, K.G., Hellmann, R. (2011). Influence of amorphous silica layer formation on the dissolution rate of olivine at 90°C and elevated pCO_2, *Chemical Geology 284*, 193–209.

Fallick, A. E., Ilich, M., and Russell, M. J. (1991), A stable isotope study of the magnesite deposits associated with the Alpine-type ultramafic rocks of Yugoslavia, *Economic Geology*, *86*(4), 847–861.

Foster, L., Eggleton, R. A., and Roach, I. C. (2002), The Marlborough nickel laterite deposits, vol. 1, edited by I. C. Roach, pp. 33–36, CRC LEME.

Gerdemann, S., Dahlin, D., O Connor, W., and Penner, L. (2003), Carbon dioxide sequestration by aqueous mineral carbonation of magnesium silicate minerals, *Greenhouse gas technologies. Elsevier Science, Amsterdam, The Netherlands*, 8.

Ghoneim, M., Saleem, I., and Hamdy, M. (2003), Origin of magnesite veins in serpentinites from Mount El-Rubshi and Mount El-Maiyit, Eastern Desert Egypt, *Archiwum Mineralogiczne*, 41–63.

Giammar, D., Bruant, R., and Peters, C. (2005), Forsterite dissolution and magnesite precipitation at conditions relevant for deep saline aquifer storage and sequestration of carbon dioxide, *Chemical Geology*, *217*(3-4), 257–276.

Glasser, E. (1904), *Rapport à M. le Ministre des colonies sur les richesses de la Nouvelle-Calédonie*, Dunod.

Goff, F., and Lackner, K. S. (1998), Carbon Dioxide Sequestering Using Ultramafic Rocks, *Environmental Geosciences*, *5*(3), 89–102.

Götze, J., Nasdala, L., Kleeberg, R., and Wenzel, M. (1998), Occurrence and distribution of "moganite" in agate/chalcedony: a combined micro-Raman, Rietveld, and cathodoluminescence study, *Contributions to Mineralogy and Petrology*, *133*(1), 96–105.

Graetsch, H., Flörke, O. W., and Miehe, G. (1985), The nature of water in chalcedony and opal-C from Brazilian agate geodes, *Physics and Chemistry of Minerals*, *12*, 300–306.

Griffis, R. (1972), Genesis of a magnesite deposit, Deloro Twp., Ontario, *Economic Geology*, *67*(1), 63–71.

Guthrie, G. D., Carey, J. W., Bergfeld, D., Byler, D., Chipera, S., Ziock, H. J., and Lackner, K. S. (2001), Geochemical aspects of the carbonation of magnesium silicates in an aqueous medium, *NETL Conference on Carbon Sequestration*, 14 pp.

Halls, C., and Zhao, R. (1995), Listvenite and related rocks: perspectives on terminology and mineralogy with reference to an occurrence at Cregganbaun, Co. Mayo, Republic of Ireland, *Mineralium Deposita*, *30*(3), 303–313.

Hansen, L., Dipple, G., Gordon, T., and Kellett, D. (2005), Carbonated serpentinite (listwanite) at Atlin, British Columbia: A geological analogue to carbon dioxide sequestration, *The Canadian Mineralogist*, *43*(1), 225–239.

Harrison, A.L., Power, I.M., Dipple, G.M. (2013). Accelerated Carbonation of Brucite in Mine Tailings for Carbon Sequestration, *Environmental Science & Technology*, *47*, 126–134.

Haug, T. A., Munz, I. A., and Kleiv, R. A. (2011), Importance of dissolution and precipitation kinetics for mineral carbonation, *Energy Procedia*, *4*(C), 5029–5036.

Heaney, P. (1993), A proposed mechanism for the growth of chalcedony, *Contributions to Mineralogy and Petrology*, *115*(1), 66–74.

Heaney, P., and Post, J. E. (1992), The widespread distribution of a novel silica polymorph in microcrystalline quartz varieties, *Science*, *255*(5043), 441–443.

Hellmann, R., Wirth, R., Daval, D., Barnes, J.-P., Penisson, J.-M., Tisserand, D., Epicier, T., Florin, B., Hervig, R.L. (2012). Unifying natural and laboratory chemical weathering with interfacial dissolution–reprecipitation: A study based on the nanometer-scale chemistry of fluid–silicate interfaces, *Chemical Geology, 294-295*, 203–216.

Hövelmann, J., Austrheim, H., and Jamtveit, B. (2012), Microstructure and porosity evolution during experimental carbonation of a natural peridotite, *Chemical Geology*, *334*, 254–265.

Hövelmann, J., Austrheim, H., Beinlich, A., and Anne Munz, I. (2011), Experimental study of the carbonation of partially serpentinized and weathered peridotites, *Geochimica et Cosmochimica Acta*, *75*(22), 6760–6779.

Jedrysek, M. O., and Halas, S. (1990), The origin of magnesite deposits from the Polish Foresudetic Block ophiolites: preliminary $\delta^{13}C$ and $\delta^{18}O$ investigations, *Terra Nova*, *2*(2), 154–159.

Jones, B.F., and Galàn, E. (1988) Sepiolite and palygorskite, in: Hydrous Phyllosilicates (Exclusive of Micas) (S.W. Bailey, editor). *Reviews in Mineralogy, 19*. Mineralogical Society of America, Washington D.C, pp. 631-674.

Jurković, I., Palinkaš, L. A., Garašić, V., and Palinkaš, S. S. (2012), Genesis of vein-stockwork cryptocrystalline magnesite from the Dinaride ophiolites, *Ofioliti*, *37*(1), 1–14.

Kelemen, P. B., and Matter, J. (2008), In situ carbonation of peridotite for CO_2 storage, *Proceedings of the National Academy of Sciences*, *105*, pp. 17295–17300.

Kelemen, P. B., Matter, J., Streit, E. E., Rudge, J. F., Curry, W. B., and Blusztajn, J. (2011), Rates and Mechanisms of Mineral Carbonation in Peridotite: Natural processes and recipes for enhanced, *in situ* CO_2 capture and storage, *Annual Review of Earth and Planetary Sciences*, *39*, 545–576.

King, H.E., Plümper, O., Putnis, A. (2010). Effect of secondary phase formation on the carbonation of olivine, *Environmental Science & Technology, 44*, 6503–6509.

King, H.E., Plümper, O., Geisler, T., Putnis, A. (2011). Experimental investigations into the silicification of olivine: Implications for the reaction mechanism and acid neutralization, *American Mineralogist, 96*, 1503–1511.

Klein, E. M., and Langmuir, C. H. (1987), Global correlations of ocean ridge basalt chemistry with axial depth and crustal thickness, *Journal of Geophysical Research-Solid Earth*, *92*(B8), 8089–8115.

Klein, F., and Garrido, C. J. (2011), Thermodynamic constraints on mineral carbonation of serpentinized peridotite, *Lithos*, *126*(3), 147–160.

Krevor, S., and Lackner, K. S. (2011), Enhancing serpentine dissolution kinetics for mineral carbon dioxide sequestration, *International Journal of Greenhouse Gas Control*, *5*(4), 1073–1080.

Krishnamurti, D. (1956), Raman spectrum of magnesite, *Proceedings Mathematical Sciences*, *43*(4), 210–212.

Lacinska, A. M., and Styles, M. T. (2012), Silicified serpentinite – a residuum of a Tertiary palaeo-weathering surface in the United Arab Emirates, *Geological Magazine*, *1*(1), 1–11.

Lemaire, C. (2000), Application des spectroscopies vibrationnelles à la détection d'amiante dans les matériaux et à l'étude des serpentines, Unpublished PhD, Université de Paris 7, Paris, 157 pp.

Lin, F.-C., and Clemency, C. (1981), The dissolution kinetics of brucite, antigorite, talc, and phlogopite at room temperature and pressure, *American Mineralogist*, *66*(7-8), 801–806.

Luce, R. W., Bartlett, R. W., and Parks, G. A. (1972), Dissolution kinetics of magnesium silicates, *Geochimica et Cosmochimica Acta*, *36*(1), 35–50.

Lugli, S., Torres-Ruiz, J., Garuti, G., and Olmedo, F. (2000), Petrography and geochemistry of the Eugui magnesite deposit (Western Pyrenees, Spain): evidence for the development of a peculiar zebra banding by dolomite replacement, *Economic Geology*, *95*(8), 1775–1791.

Lund, E. H. (1960), Chalcedony and quartz crystals in silicified coral, *American Mineralogist*, *45*, 1304–1307.

Lynne, B. Y., Campbell, K. A., James, B. J., Browne, P. R. L., and Moore, J. (2007), Tracking crystallinity in siliceous hot-spring deposits, *American Journal of Science*, *307*(3), 612–641.

Maurizot, P., Lafoy, Y., and Poupée, M. (2002), Cartographie des formations superficielles et des aléas mouvements de terrain en Nouvelle-Calédonie, Zone du Koniambo, *BRGM Public Report*, (1:33000).

Muñoz, M., Pascarellib, S., Aquilantib, G., Naryginac, O., Kurnosovc, A., Dubrovinskyc, L., 2008. Hyperspectral μ-XANES mapping in the diamond-anvil cell: analytical procedure applied to the decomposition of (Mg, Fe)-ringwoodite at the upper/lower mantle boundary. High Pressure Research 28, 665–673.

O'Hanley, D. S. (1996), *Serpentinites: records of tectonic and petrological history*, Oxford University Press, 270 pp.

Ohmoto, H., Watanabe, Y., Kumazawa, K. (2004), Evidence from massive siderite beds for a CO_2-rich atmosphere before ~ 1.8 billion years ago, *Nature, 429*, 395–399.

Oskierski, H. C., Bailey, J. G., Kennedy, E. M., Jacobsen, G., Ashley, P. M., and Dlugogorski, B. Z. (2012), Formation of weathering-derived magnesite deposits in the New England Orogen, New South Wales, Australia: Implications from mineralogy, geochemistry and genesis of the Attunga magnesite deposit, *Mineralium Deposita*, doi:10.1007/s00126-012-0440-5.

Pefrov, V. P., Vakanjac, B., Joksimović, D., Zekić, M., and Lapcević, I. (1980), Magnesite deposits of Serbia and their origin, *International Geology Review*, *22*(5), 497–510.

Plümper, O., Royne, A., Magraso, A., and Jamtveit, B. (2012). The interface-scale mechanism of reaction-induced fracturing during serpentinization. *Geology, 40(12)*, 1103–1106.

Podwojewski, P. (1995), The occurrence and interpretation of carbonate and sulfate minerals in a sequence of Vertisols in New Caledonia, *Geoderma*, *65*(3-4), 223–248.

Pohl, W. (1990), Genesis of magnesite deposits — models and trends, *Geologische Rundschau*, *79*, 291–299.

Pop, D., Constantina, C., Tătar, D., and Kiefer, W. (2004), Raman spectroscopy on gem-quality microcrystalline and amorphous silica varieties from Romania, *Studia UBB, Geologia*, *49*(1), 41–52.

Power, I.M., Wilson, S.A., Small, D.P., Dipple, G.M., Wan, W., Southam, G. (2011). Microbially Mediated Mineral Carbonation: Roles of Phototrophy and Heterotrophy. *Environmental Science & Technology, 45*, 9061–9068.

Prigiobbe, V., Hänchen, M., Costa, G., Baciocchi, R., and Mazzotti, M. (2009), Analysis of the effect of temperature, pH, CO_2 pressure and salinity on the olivine dissolution kinetics, *Energy Procedia*, *1*(1), 4881–4884.

Prinzhoffer, A. (1981). Structure et pétrologie d'un cortège ophiolitique: le massif du Sud (Nouvelle-Calédonie): Unpublished thesis, E.N.S.M. Paris, 306 pp.

Quesnel, B., Gautier, P., Boulvais, P., Cathelineau, M., Maurizot, P., Cluzel, D., Ulrich, M., Guillot, S., Lesimple, S., Couteau, C., (2013). Syn-tectonic, meteoric water-derived carbonation of the New Caledonia peridotite nappe. *Geology*, 41, 1063–1066.

Renforth, P., Washbourne, C.L., Taylder, J., Manning, D.A.C. (2011). Silicate Production and Availability for Mineral Carbonation. *Environmental Science & Technology, 45*, 2035–2041.

Rodgers, K. A., and Cressey, G. (2001), The occurrence, detection and significance of moganite (SiO_2) among some silica sinters, *Mineralogical Magazine*, *65*(2), 157–167.

Rudge, J. F., Kelemen, P. B., and Spiegelman, M. (2010), A simple model of reaction-induced cracking applied to serpentinization and carbonation of peridotite, *Earth and Planetary Sciences Letters*, *291*(1-4), 215–227.

Ruiz-Agudo, E., Putnis, C.V., Rodriguez-Navarro, C., Putnis, A. (2012). Mechanism of leached layer formation during chemical weathering of silicate minerals, *Geology, 40*, 947–950.

Saldi, G.D., Daval, D., Morvan, G., Knauss, K.G. (2013). The role of Fe and redox conditions in olivine carbonation rates: An experimental study of the rate limiting reactions at 90 and 150°C in open and closed systems, *Geochimica et Cosmochimica Acta, 118*, 157–183.

Schellart, W., Lister, G., and Toy, V. (2006), A Late Cretaceous and Cenozoic reconstruction of the Southwest Pacific region: tectonics controlled by subduction and slab rollback processes, *Earth Science Reviews*, *76*(3-4), 191–233.

Schulze, R., Hill, M., Field, R., Papin, P., Hanrahan, R., and Byler, D. (2004), Characterization of carbonated serpentine using XPS and TEM, *Energy Conversion and Management*, *45*(20), 3169–3179.

Sévin, B., Ricordel Prognon, C., Quesnel, F., Cluzel, D., Lesimple, S., Maurizot, P., (2012). First palaeomagnetic dating of ferricrete in New Caledonia: new insight on the morphogenesis and palaeoweathering of "Grande Terre", *Terra Nova, 24*, 77–85.

Sherlock, R., and Logan, M. (1995), Silica-carbonate alteration of serpentinite; implications for the association of mercury and gold mineralization in Northern California, *Exploration and Mining Geology*, *4*(4), 395–409.

Sipilä, J., Teir, S., and Zevenhoven, R. (2008), Carbon dioxide sequestration by mineral carbonation: Literature review update 2005–2007, *Åbo Akademi Rep. VT*, *1,* 59 pp.

Stanger, G. (1985), Silicified serpentinite in the Semail nappe of Oman, *Lithos*, *18*, 13–22.

Teir, S., Eloneva, S., Fogelholm, C.-J., and Zevenhoven, R. (2009), Fixation of carbon dioxide by producing hydromagnesite from serpentinite, *Applied Energy*, *86*(2), 214–218.

Teir, S., Kuusik, R., Fogelholm, C., and Zevenhoven, R. (2007), Production of magnesium carbonates from serpentinite for long-term storage of CO2, *International Journal of Mineral Processing*, *85*(1-3), 1–15.

Trescases, J. (1973), Weathering and geochemical behaviour of the elements of ultramafic rocks in New Caledonia, *Bureau of Mineral Resources Geology and Geophysics Department of Minerals and Energy Canberra Bulletin*, *141*, 149–161.

Ulrich, M. (2010), Péridotites et serpentinites du complexe ophiolitique de la Nouvelle-Calédonie, Unpublished Thesis, Université de la Nouvelle-Calédonie et Université de Grenoble, 253 pp.

Ulrich, M., Picard, C., Guillot, S., Chauvel, C., Cluzel, D., and Meffre, S. (2010), Multiple melting stages and refertilization as indicators for ridge to subduction formation: The New Caledonia ophiolite, *Lithos*, *115*, 223–236.

van Noort, R., Spiers, C. J., Drury, M. R., and Kandianis, M. T. (2013), Peridotite dissolution and carbonation rates at fracture surfaces under conditions relevant for in situ mineralization of CO_2, *Geochimica et Cosmochimica Acta*, *106*(C), 1–24.

Whattam, S. A. (2009), Arc-continent collisional orogenesis in the SW Pacific and the nature, source and correlation of emplaced ophiolitic nappe components, *Lithos*, *113*(1), 88–114.

Whattam, S. A., Malpas, J., Ali, J., and Smith, I. E. (2008), New SW Pacific tectonic model: Cyclical intraoceanic magmatic arc construction and near-coeval emplacement along the Australia-Pacific margin in the Cenozoic, *Geochemistry Geophysics Geosystems*, *9*(3), doi: 10.1029/2007GC001710.

Williams, L. A., and Crerar, D. A. (1985), Silica Diagenesis, II. General Mechanisms, *Journal of Sedimentary Research*, *55*(3), 312–321.

Williams, L. A., Parks, G., and Crerar, D. A. (1985), Silica Diagenesis, I. Solubility Controls, *Journal of Sedimentary Petrology*, *55*(3), 301–311.

Wilson, S. A., Dipple, G. M., Power, I. M., Thom, J. M., Anderson, R. G., Raudsepp, M., Gabites, J. E., and Southam, G. (2009), Carbon dioxide fixation within mine wastes of ultramafic-hosted ore deposits: Examples from the Clinton Creek and Cassiar chrysotile deposits, Canada, *Economic Geology*, *104*(1), 95–112.

Yaliçin, H., and Bozkaya, Ö. (2004), Ultramafic-rock-hosted vein sepiolite occurrences in the Ankara Ophiolitic Melange, Central Anatolia, Turkey, *Clays and Clay Minerals*, *52*(2), 227–239.

Zedef, V., Russell, M., Fallick, A., and Hall, A. (2000), Genesis of vein stockwork and sedimentary magnesite and hydromagnesite deposits in the ultramafic terranes of southwestern Turkey: a stable isotope study, *Economic Geology*, *95*(2), 429.

Figure captions

Figure 1: Localization of the main ophiolitic occurrences composing the Peridotite Nappe. Simplified geological map of the Koniambo massif is modified from Maurizot *et al.* (2002).

Figure 2: a, b, c) Snow-white colored magnesite veins crystallized in massive serpentinite blocs, Koniambo massif. Magnesite show a typical cauliflower texture and is closely associated with silica veins (in brown). **d)** Typical sample of carbonated serpentinite. Orange dashed line square localizes the mapped area by µ-XRF presented in Figures 6 to 8 and in Figures S2 and S3.

Figure 3: Typical XRD patterns of serpentinite and magnesite. Liz: Lizardite; Chr: Chromite; Opl: Opal; Mgs: Magnesite; Mgt: Magnetite; Ctl: Chrysotile. Numbers upon the magnesite peaks correspond to *d* values, given in Å.

Figure 4: a) Microphotography under polarized light illustrating the development of magnesite and silica in serpentinite. **b)** Microphotography under crossed-polarized light showing the development of magnesite along the rims of serpentine grains (indicated by the red arrows). Notice that the serpentinization also affects the orthopyroxene **c)** Magnesite grain aggregates surrounded by colloform amorphous silica gel. Associated brown and fibrous mineral corresponds to sepiolite (observation under polarized light). **d)** Nucleation of magnesite grain on serpentine surface surrounded by colloform amorphous silica gel. Black dots inside of the serpentine grain correspond to magnetite (observation under crossed-polarized light). **e)** Microtextures of a silica vein under polarized light (mesh: serpentine mesh; #1: opal-CT, #2 and #3: Chalcedony; identifications made by raman spectroscopy, see Figure 5). **e)** Same as e) under crossed-polarized light. Mineral abbreviations: Mgs: magnesite; Mgt: Magnetite; Opx: Orthopyroxene; Sep: sepiolite; Srp: serpentine

Figure 5: Typical Raman spectra observed for serpentine (lizardite and polygonal), chalcedony, opal-CT and magnesite composing the serpentinite sole of the New Caledonia ophiolite.

Figure 6: Quantitative chemical maps of MgO, SiO_2 and Fe_2O_3 (in wt.%) calculated on the basis of μ-XRF measurements (EDAX Eagle III). Complete procedure for the map calculation is detailed in the text.

Figure 7: Spatial repartition and quantification of mineral phases (in %) calculated on each pixel of the mapped area (Figure 2d), based on μ-XRF measurements (EDAX Eagle III). Square-delimited regions correspond to areas used to construct correlation diagrams in Figure 8.

Figure 8: Correlation diagrams (represented as density fields) between serpentine, magnesite and silica based on the phase distribution maps for the two square-delimited regions in Figure 8. *n* corresponds to the total number of pixels composing each region. Colorbar values correspond to the number of pixels in one grid cell of a size of 5% by 5%.

Figure 9: Microphotography under polarized light and schematic representation of the partially carbonated serpentine grain (corresponding to the Region 2 in Figure 7).

Figure 10: Schematic sketch of coupled carbonation-silicification in dissolution-precipitation processes. **a)** High pH meteoric waters (yellow arrows) percolating in serpentinite porosity start to dissolve the serpentine. **b)** In zones of high fluid flow (see the text for more details), dissolution of the serpentine surface releases Mg^{2+} cations (white arrows) that migrate to zones of reduced fluid flow, leaving behind a Si-rich layer. Iron released during this dissolution step immediately precipitates as magnetite due to local oxidizing conditions favored by the constant renewal of water that characterizes zones of high fluid flow (Andreani *et al.*, 2009). **c)** Magnesite precipitates at the expense of serpentine surface in zones of reduced fluid flow due to local supersaturation and more reducing conditions. Released silica may precipitate as amorphous silica interstitially to magnesite aggregates, but increasing pH as the carbonation proceeds leads to its solubilization and subsequent migration in the serpentine mesh (orange dashed arrows). **d)** Silica, in aqueous form, propagates in the serpentine mesh and finally precipitates in amorphous opal A subsequently evolving to opal CT, chalcedony and ultimately quartz. Complete serpentine replacement in a magnesite+silica assemblage may occur. Alternatively, the growing of magnesite may lead to the closure of initial porosity, preventing additional fluid circulations and thus ending the carbonation process before going to completion (Hövelmann *et al.*, 2012).

Table

Table 1: *In situ* concentration measurements by μ-XRF for serpentine, magnesite, silica, sepiolite, magnetite and chromite used for the calculation of quantitative maps shown in Figure 6 (see also electronic supplements, Figure S6).

Elements	Serpentine	Magnesite	Silica	Magnetite	Sepiolite	Chromite
MgO	40.25	46.84	-	-	24.72	12.34
Al_2O_3	0.41	-	-	-	0.46	23.22
SiO_2	43.60	0.39	100.00	-	62.66	0.08
K_2O	-	-	-	-	0.01	0.01
CaO	-	0.54	-	-	0.2	0.07
TiO_2	0.01	-	-	-	0.02	-
Cr_2O_3	0.02	-	-	-	0.02	48.20
MnO	0.03	-	-	-	0.67	0.20
FeO	2.51	0.02	-	100.00	0.55	15.82
NiO	0.17	-	-	-	0.11	0.06
CO_2	-	52.21	-	-	-	-
H_2O	13.00	-	-	-	10.58	-
Total	100.00	100.00	100.00	100.00	100.00	100.00

Supplementary figure captions

Figure S1: Raman spectra of brown chalcedony (Silica #2, Figure 4) and white chalcedony (Silica #3, Figure 4). Both only differ by the intensity of the moganite band (501) which is significantly higher in the white chalcedony.

Figure S2: RGB (for Red-Green-Blue) map calculated by the superposition of the three phase maps shown in Figure 7. One color is attributed to each phase (Red: Magnesite; Green: Serpentine; Blue: Silica), in order to highlight the relationship between mineral phases. Pixels characterized by a mix of green and blue show the progressive silicification of the serpentine mesh. Greenish to brownish pixels (mix of red and green) correspond to partially carbonated serpentine grains.

Figure S3: Progressive silicification of the serpentine mesh illustrated by Raman spectroscopy.

Figure S4: μ-XRF maps of elemental concentrations based on ROI (region of interest) measurement at element K-edge. These maps correspond to raw data used for the calculation of mineral phase maps (in %) shown in Figure 6 and Figure S5, and quantitative maps shown in Figure 6 and Figure S6.

Figure S5: Maps of mineral phases calculated calculated on the basis of μ-XRF measurements (EDAX Eagle III). The «Total» map corresponds to the sum of phase maps and is used to verify the consistency of the calculation (each pixel of the map have to be close to 100 %).

Figure S6: Quantitative maps (in wt.%) calculated on the basis of μ-XRF measurements (EDAX Eagle III). The «Total» map corresponds to the sum of quantitative maps. Map of H_2O +CO_2, elements that cannot be measured by μ-XRF, is calculated by subtracting the Total map to 100.

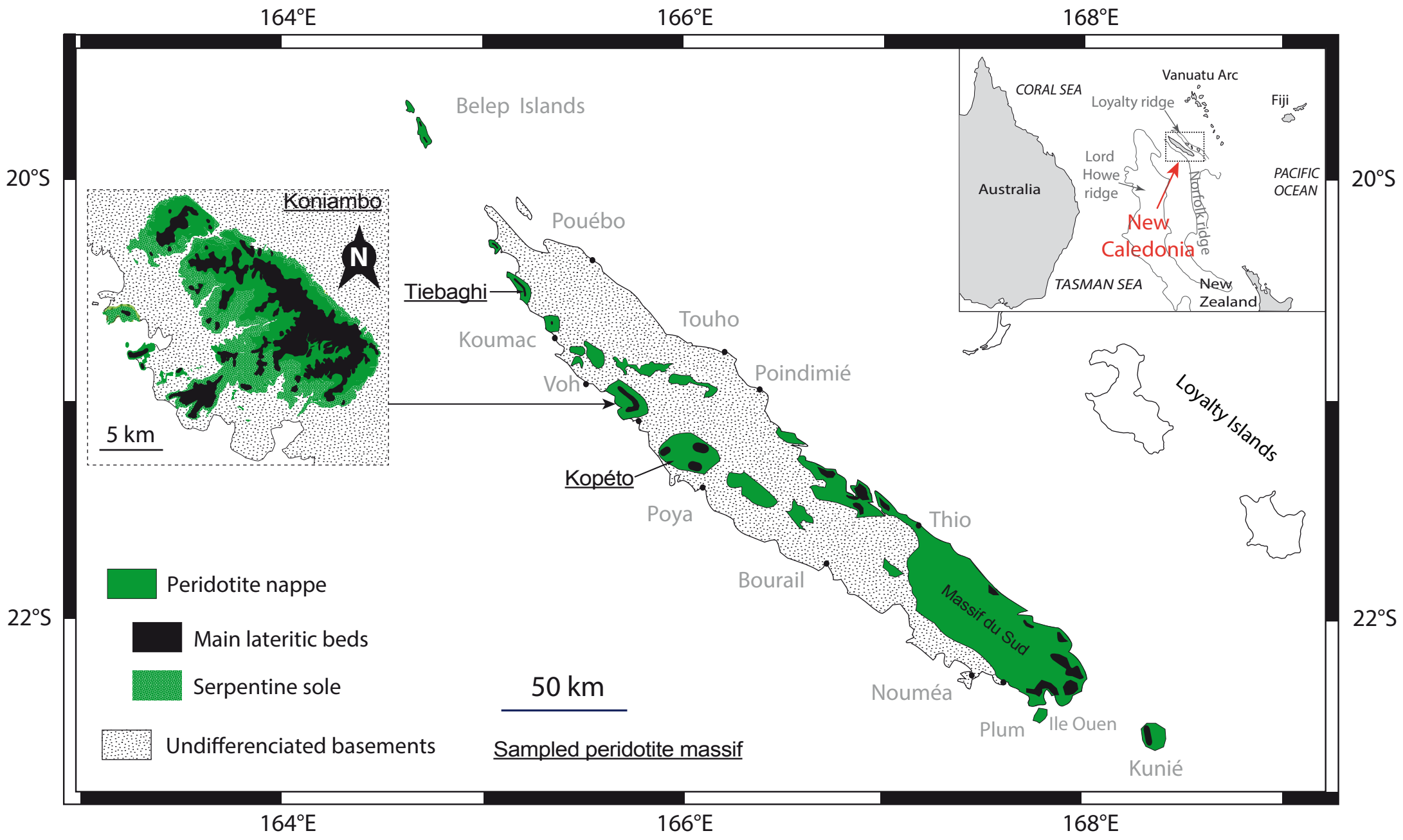
164°E
166°E
168°E
20°S
22°S
Belep Islands
Koniambo
N
5 km
Pouébo
Tiebaghi
Touho
Koumac
Poindimié
Voh
Kopéto
Poya
Thio
Bourail
Massif du Sud
Nouméa
Plum
Ile Ouen
Kunié
Loyalty Islands
Peridotite nappe
Main lateritic beds
Serpentine sole
Undifferenciated basements
50 km
Sampled peridotite massif
CORAL SEA
Vanuatu Arc
Loyalty ridge
Fiji
Lord Howe ridge
Australia
PACIFIC OCEAN
Norfolk ridge
New Caledonia
TASMAN SEA
New Zealand

a

b

Mgs

Srp

SiO_2

c

Srp

Mgs

d

Srp

Mgs + SiO_2

1 cm

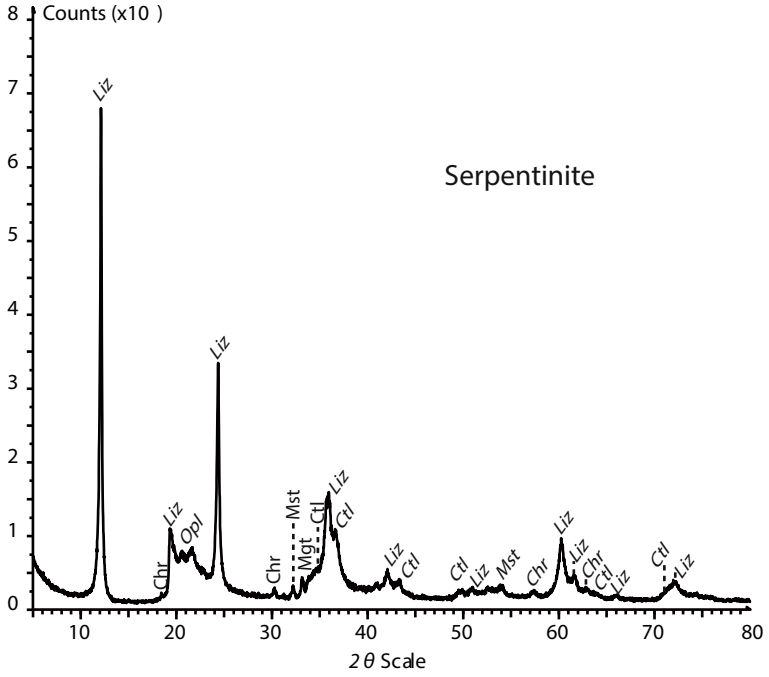
Counts (x10)
Serpentinite
Liz
Opl
Chr
Mst
Mgt
Ctl
2θ Scale

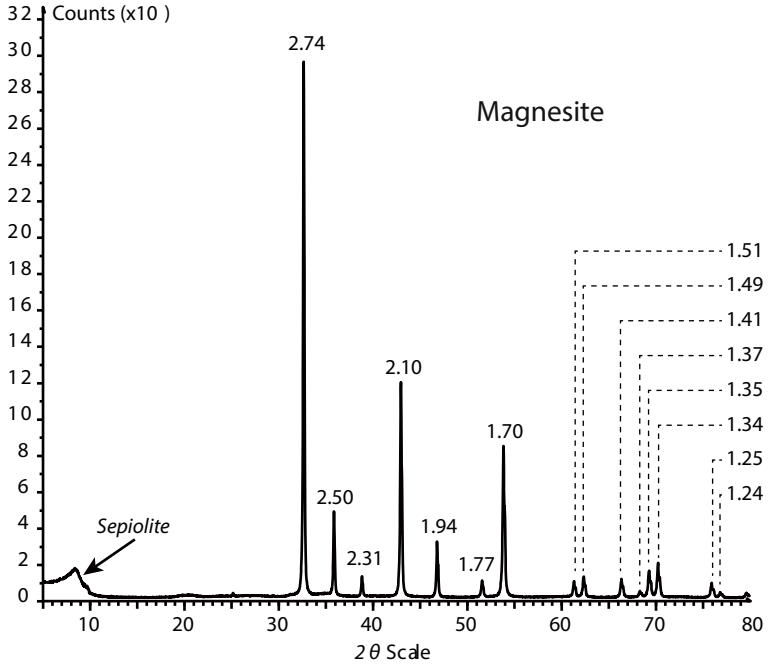
Counts (x10)
Magnesite
Sepiolite
2.74
2.50
2.31
2.10
1.94
1.77
1.70
1.51
1.49
1.41
1.37
1.35
1.34
1.25
1.24
2θ Scale

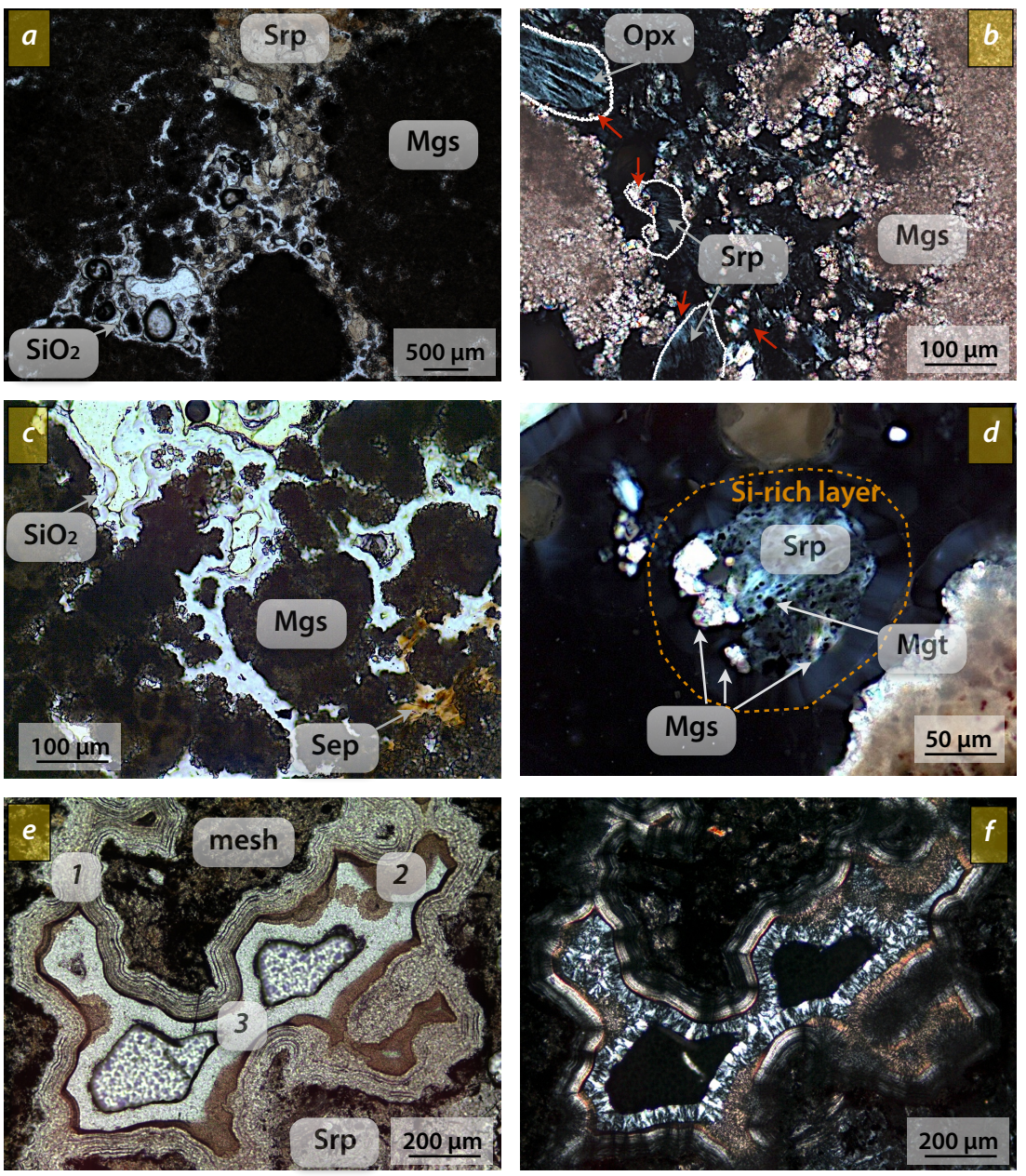
a
Srp
Mgs
SiO2
500 μm
b
Opx
Srp
Mgs
100 μm
c
SiO2
Mgs
100 μm
Sep
d
Si-rich layer
Srp
Mgt
Mgs
50 μm
e
mesh
1
2
3
Srp
200 μm
f
200 μm

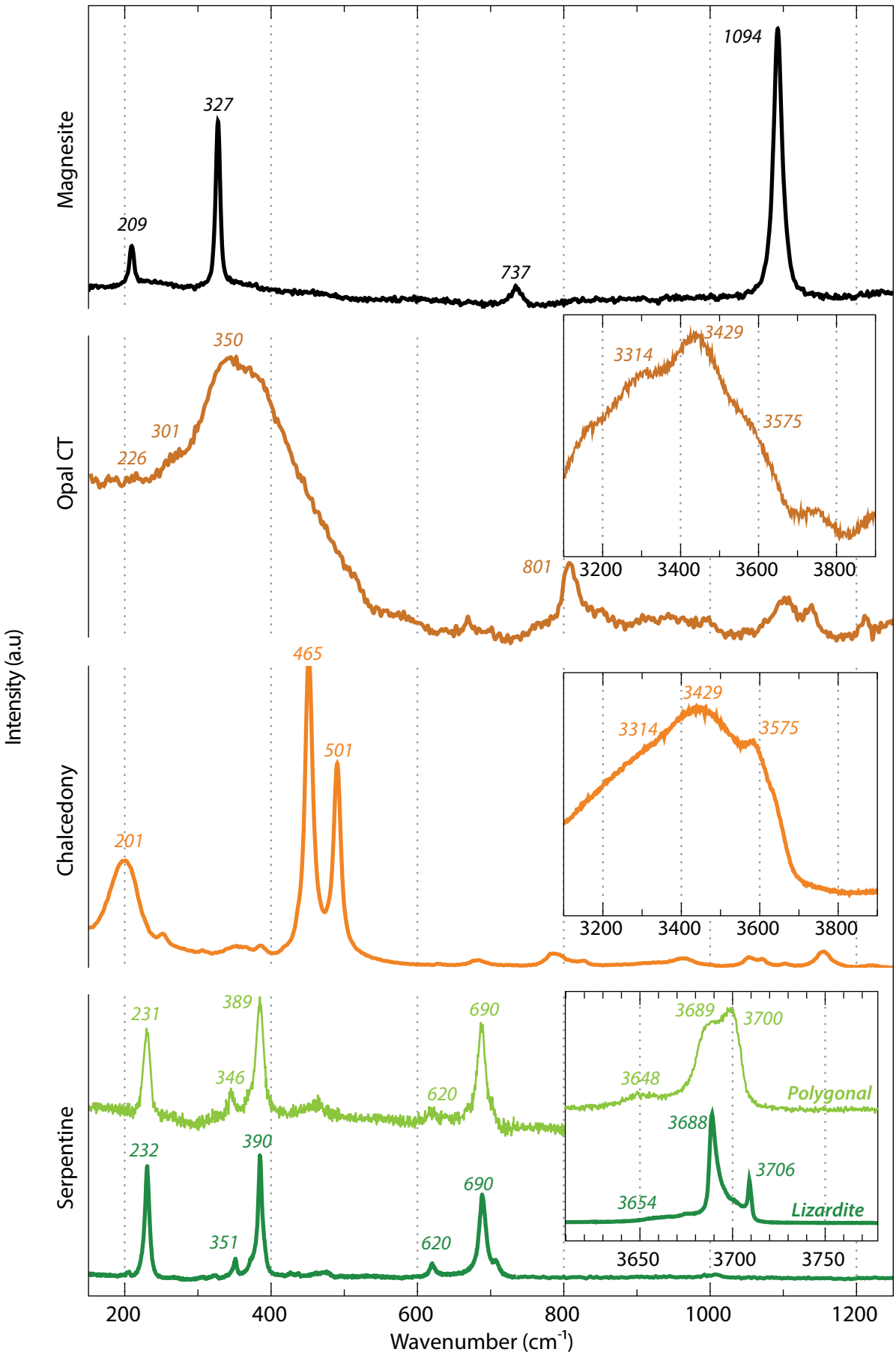
Magnesite
209
327
737
1094
Opal CT
226
301
350
801
3314
3429
3575
3200
3400
3600
3800
Chalcedony
201
465
501
3314
3429
3575
3200
3400
3600
3800
Serpentine
231
389
346
620
690
3689
3700
3648
Polygonal
232
390
351
620
690
3688
3706
3654
Lizardite
3650
3700
3750
Intensity (a.u)
200
400
600
800
1000
1200
Wavenumber (cm-1)

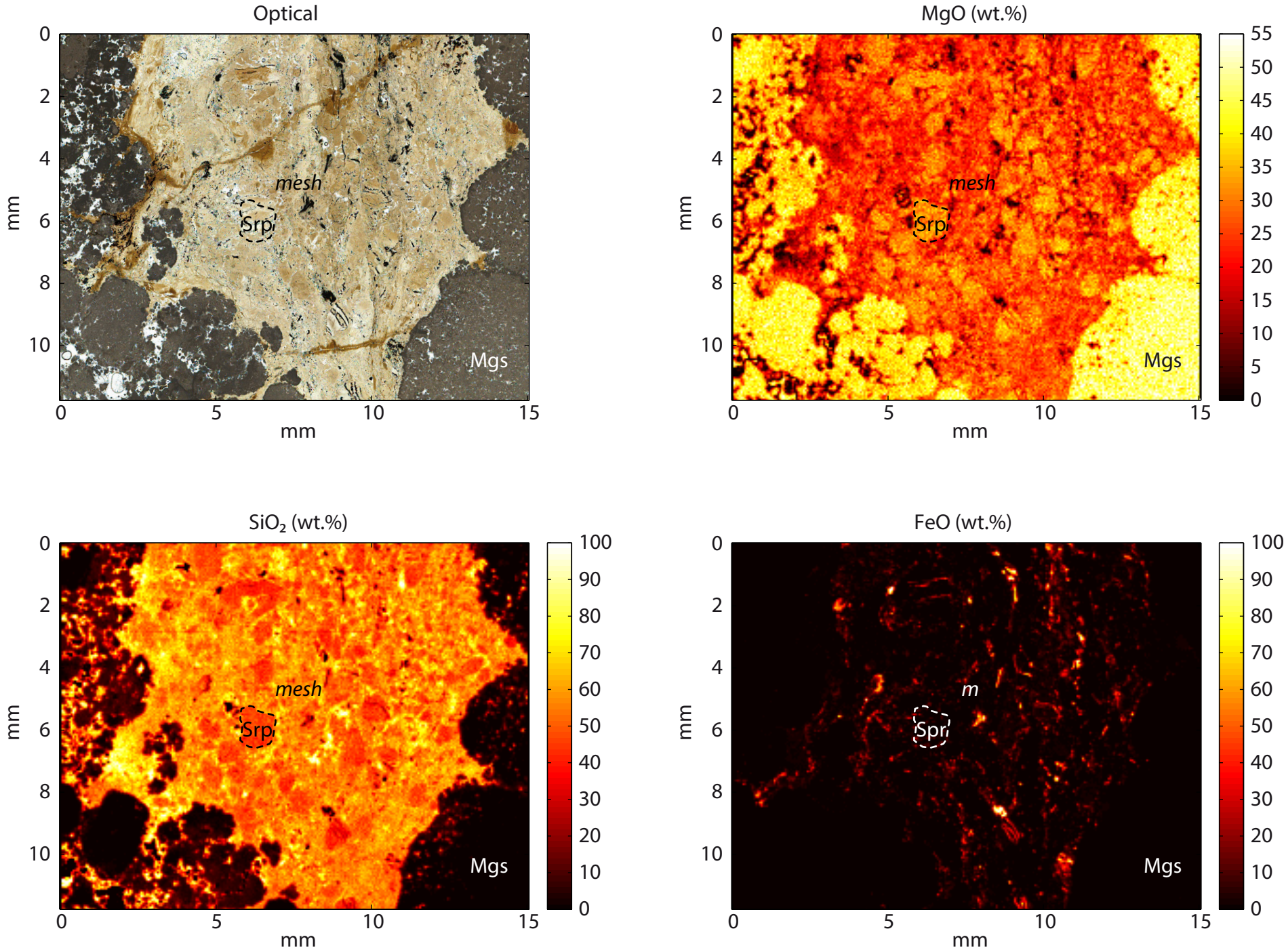
Optical
mesh
Srp
Mgs
mm
MgO (wt.%)
mesh
Srp
Mgs
mm
SiO2 (wt.%)
mesh
Srp
Mgs
mm
FeO (wt.%)
m
Spr
Mgs
mm

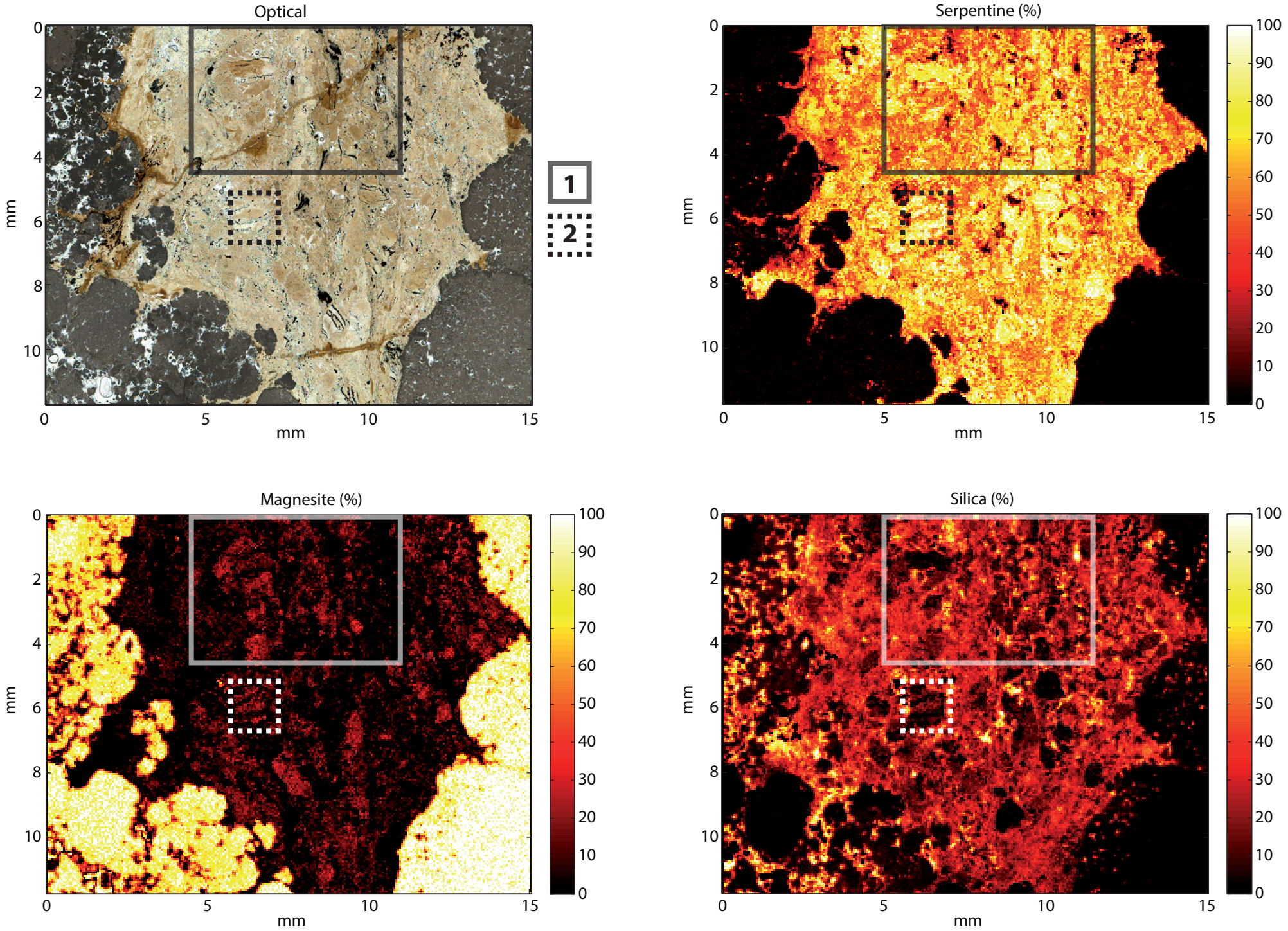
Optical
Serpentine (%)
Magnesite (%)
Silica (%)
mm
0
2
4
6
8
10
5
15
100
90
80
70
60
50
40
30
20
10
1
2

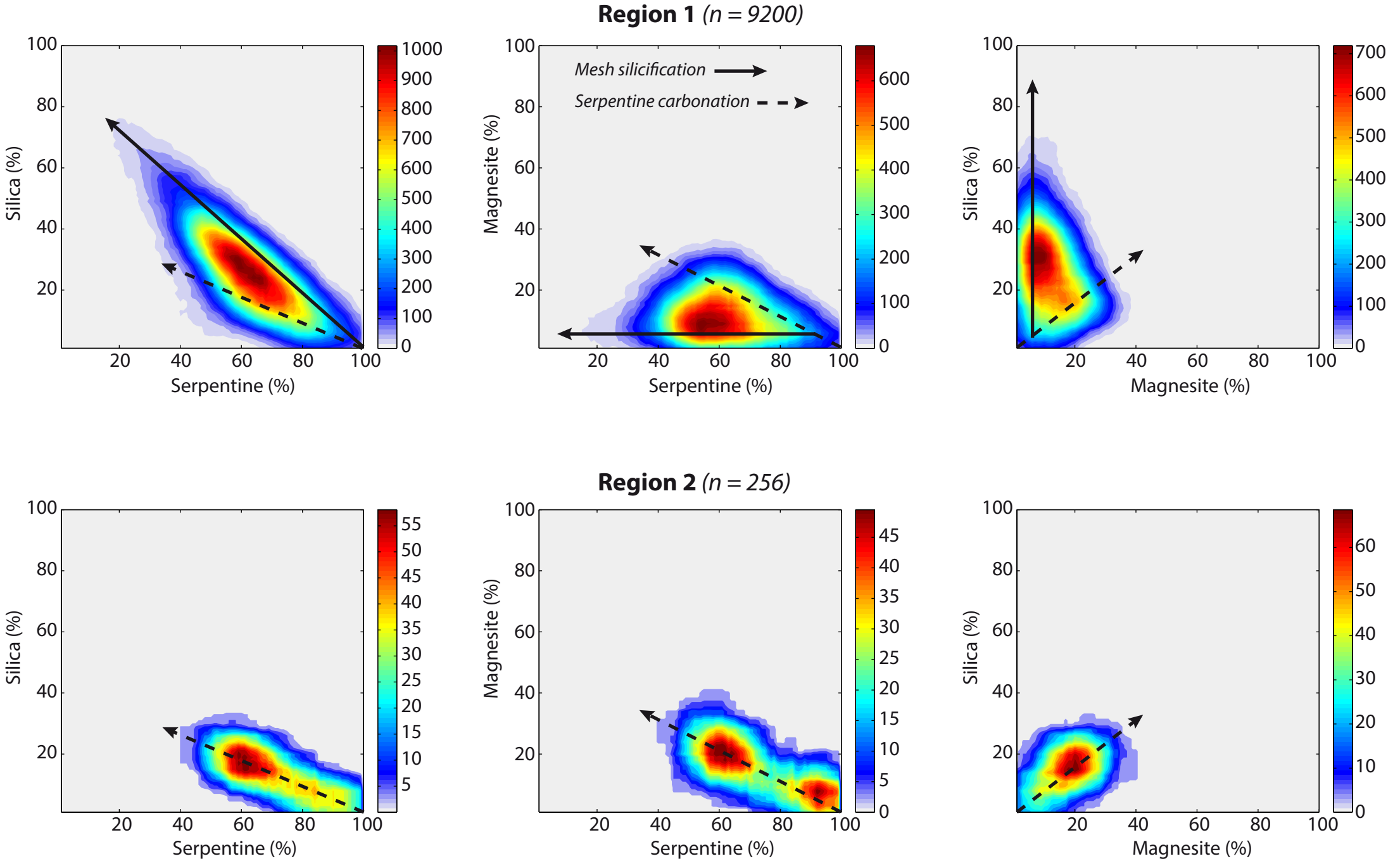
Region 1 (n = 9200)
Region 2 (n = 256)
Mesh silicification
Serpentine carbonation
Silica (%)
Serpentine (%)
Magnesite (%)
Serpentine (%)
Silica (%)
Magnesite (%)
Silica (%)
Serpentine (%)
Magnesite (%)
Serpentine (%)
Silica (%)
Magnesite (%)

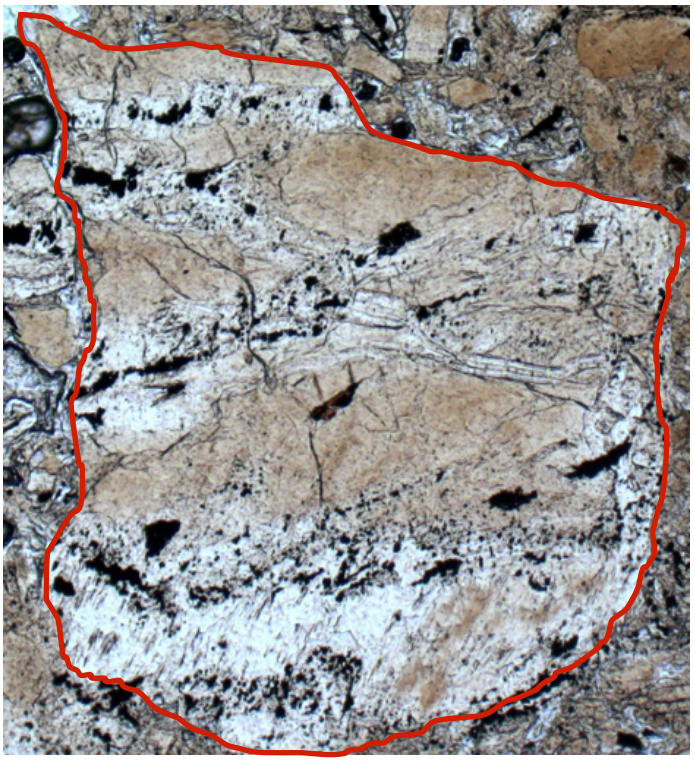

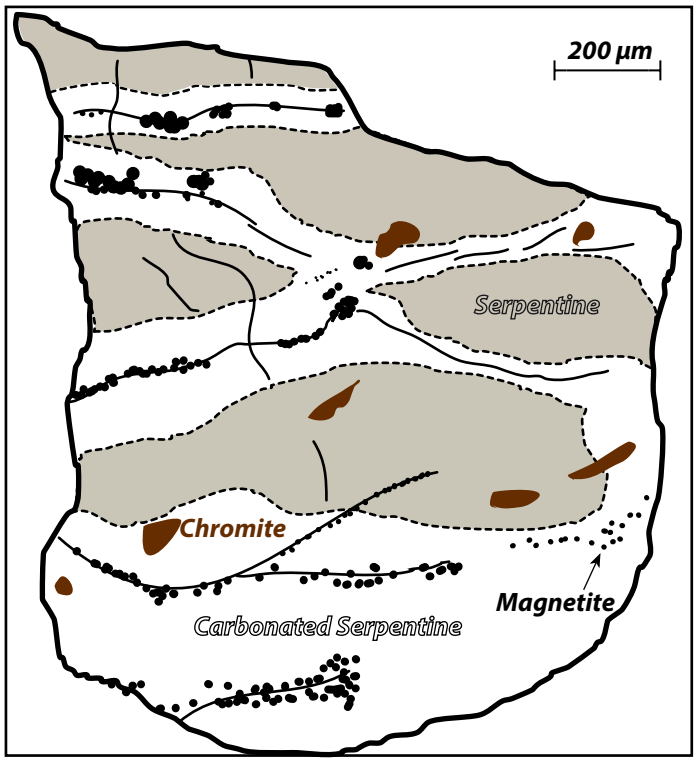
200 µm
Serpentine
Chromite
Magnetite
Carbonated Serpentine

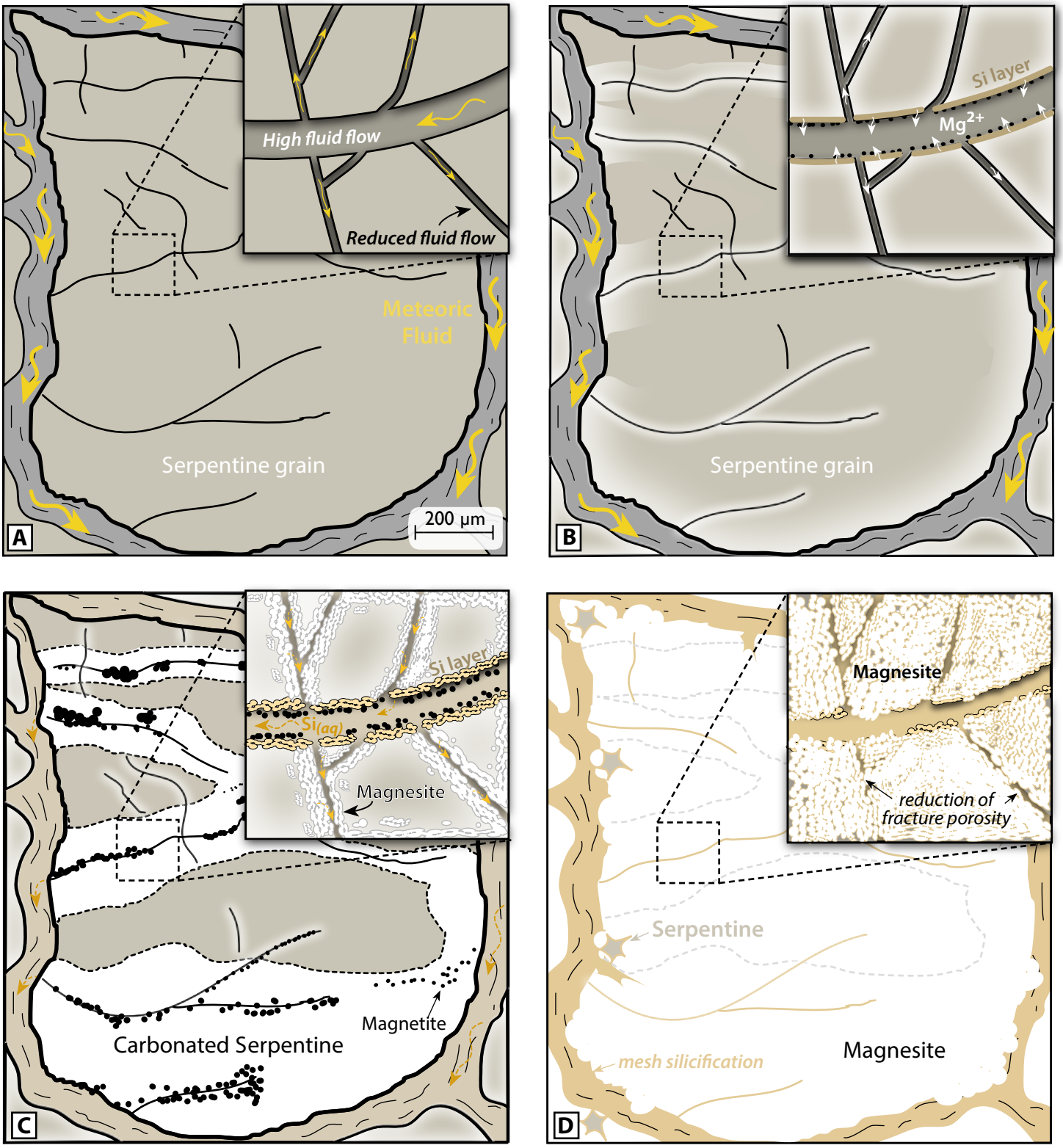
High fluid flow
Reduced fluid flow
Meteoric Fluid
Serpentine grain
200 µm
A
Si layer
Mg2+
Serpentine grain
B
Si layer
Si(aq)
Magnesite
Magnetite
Carbonated Serpentine
C
Magnesite
reduction of fracture porosity
Serpentine
mesh silicification
Magnesite
D

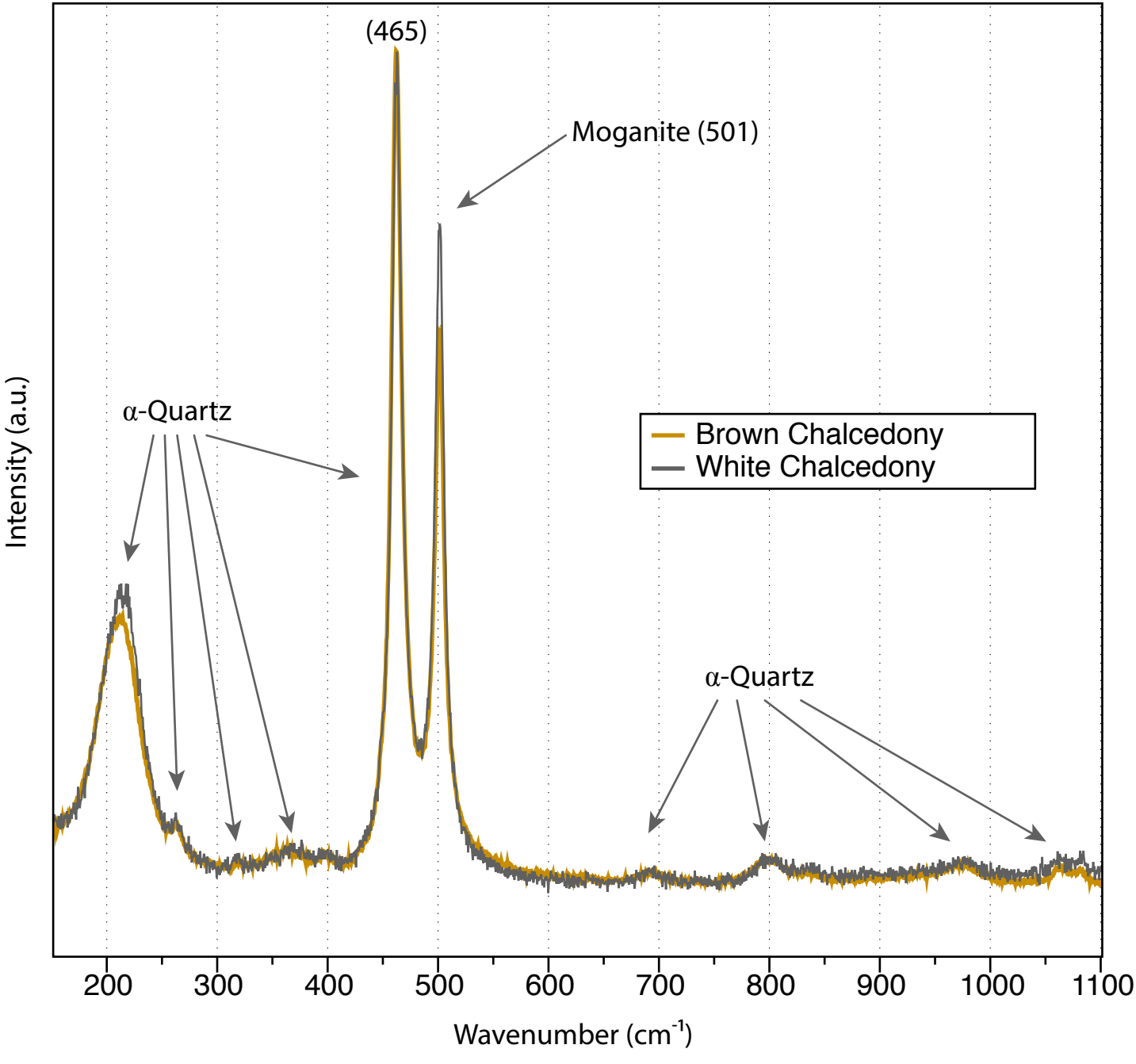
(465)
Moganite (501)
α-Quartz
α-Quartz
Brown Chalcedony
White Chalcedony
Intensity (a.u.)
200
300
400
500
600
700
800
900
1000
1100
Wavenumber (cm-1)

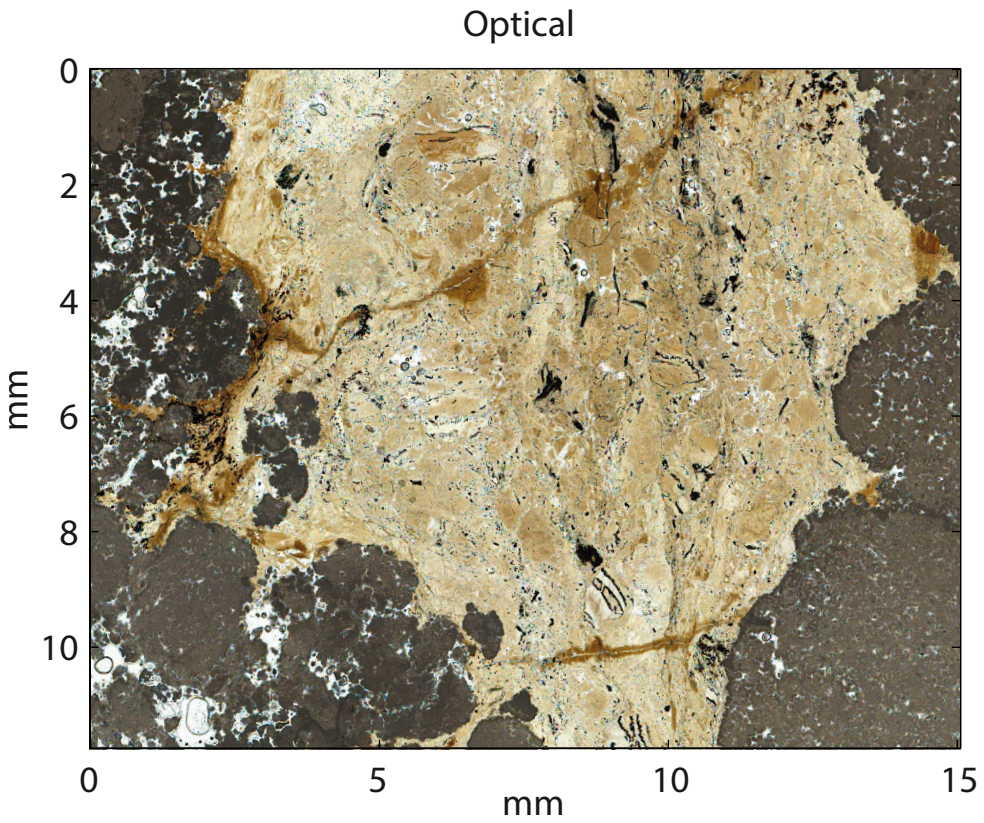
Optical
0
2
4
6
8
10
mm
0
5
10
15
mm

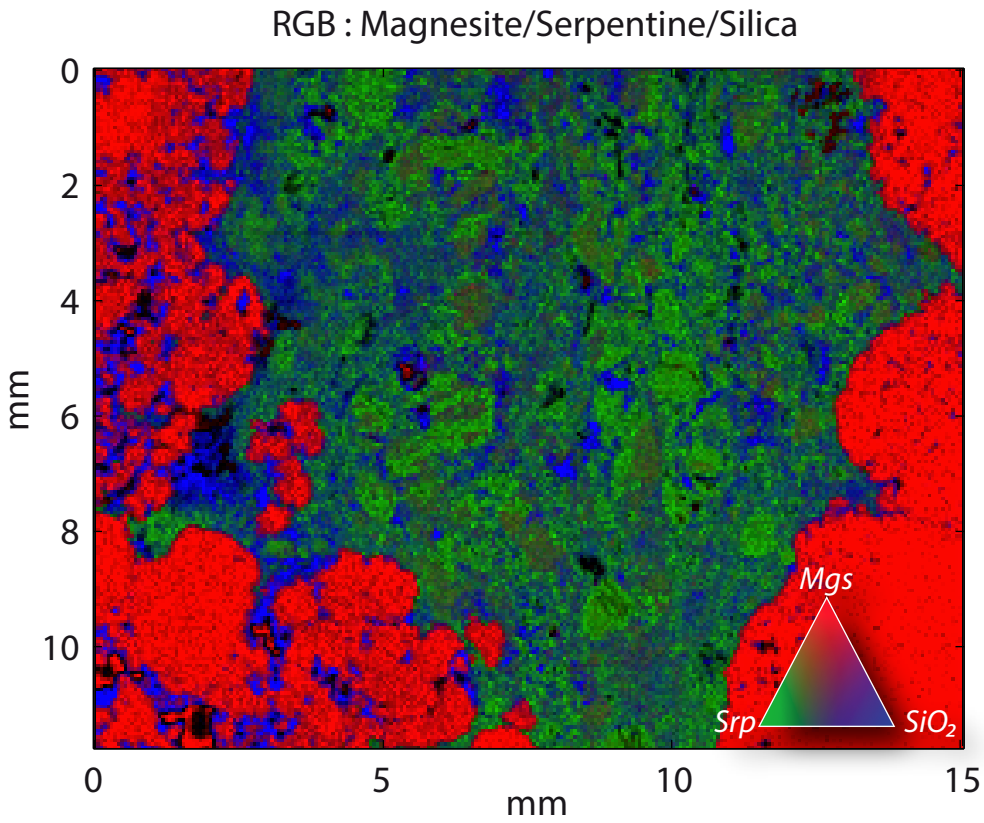
RGB : Magnesite/Serpentine/Silica
0
2
4
6
8
10
mm
0
5
10
15
mm
Mgs
Srp
SiO2

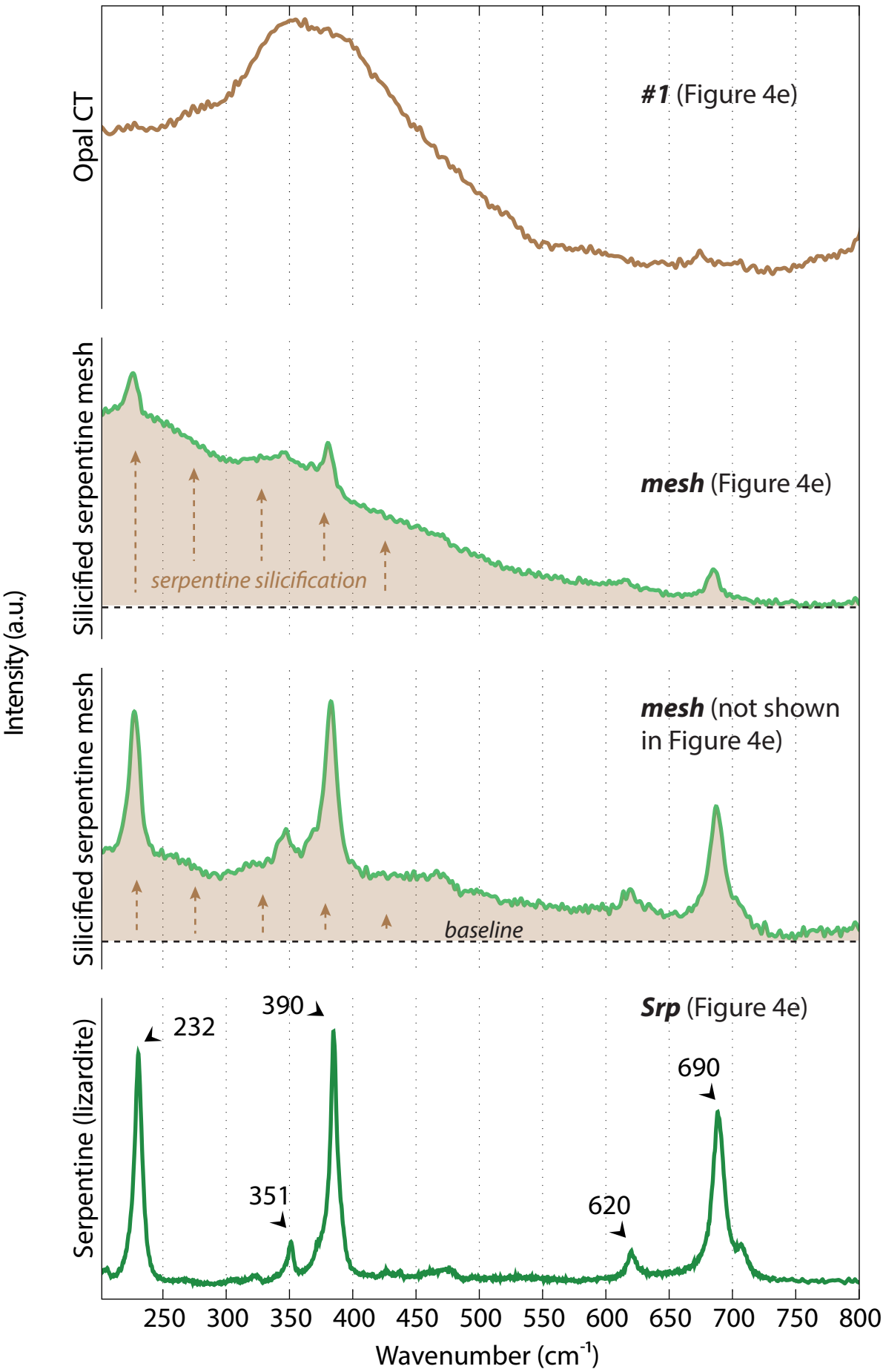
Opal CT
#1 (Figure 4e)
Silicified serpentine mesh
mesh (Figure 4e)
serpentine silicification
Silicified serpentine mesh
mesh (not shown in Figure 4e)
baseline
Serpentine (lizardite)
Srp (Figure 4e)
232
390
351
620
690
Intensity (a.u.)
250
300
350
400
450
500
550
600
650
700
750
800
Wavenumber (cm-1)

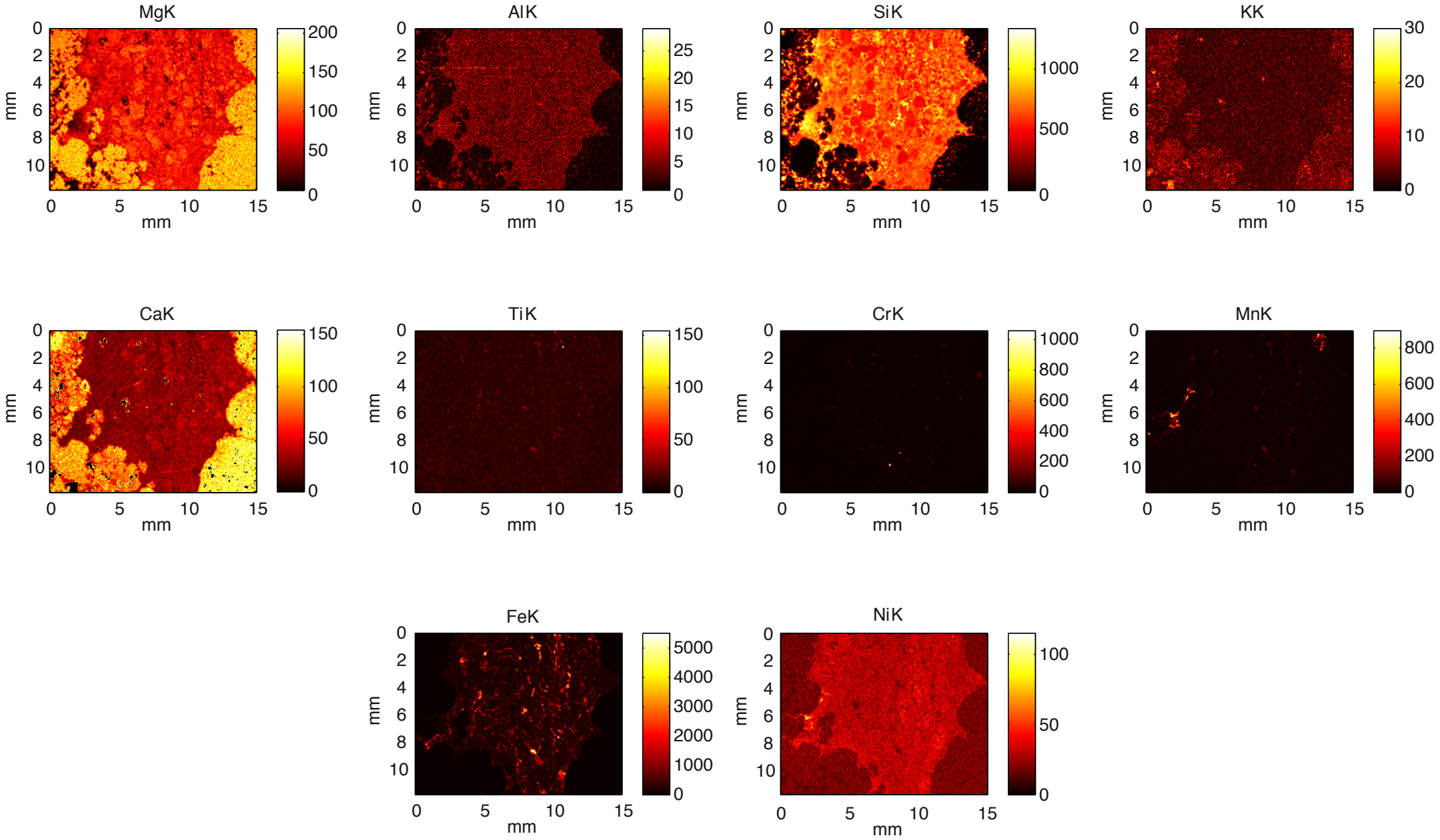
MgK
AlK
SiK
KK
CaK
TiK
CrK
MnK
FeK
NiK
mm
0
2
4
6
8
10
0
5
10
15
200
150
100
50
25
20
1000
500
30
800
600
400

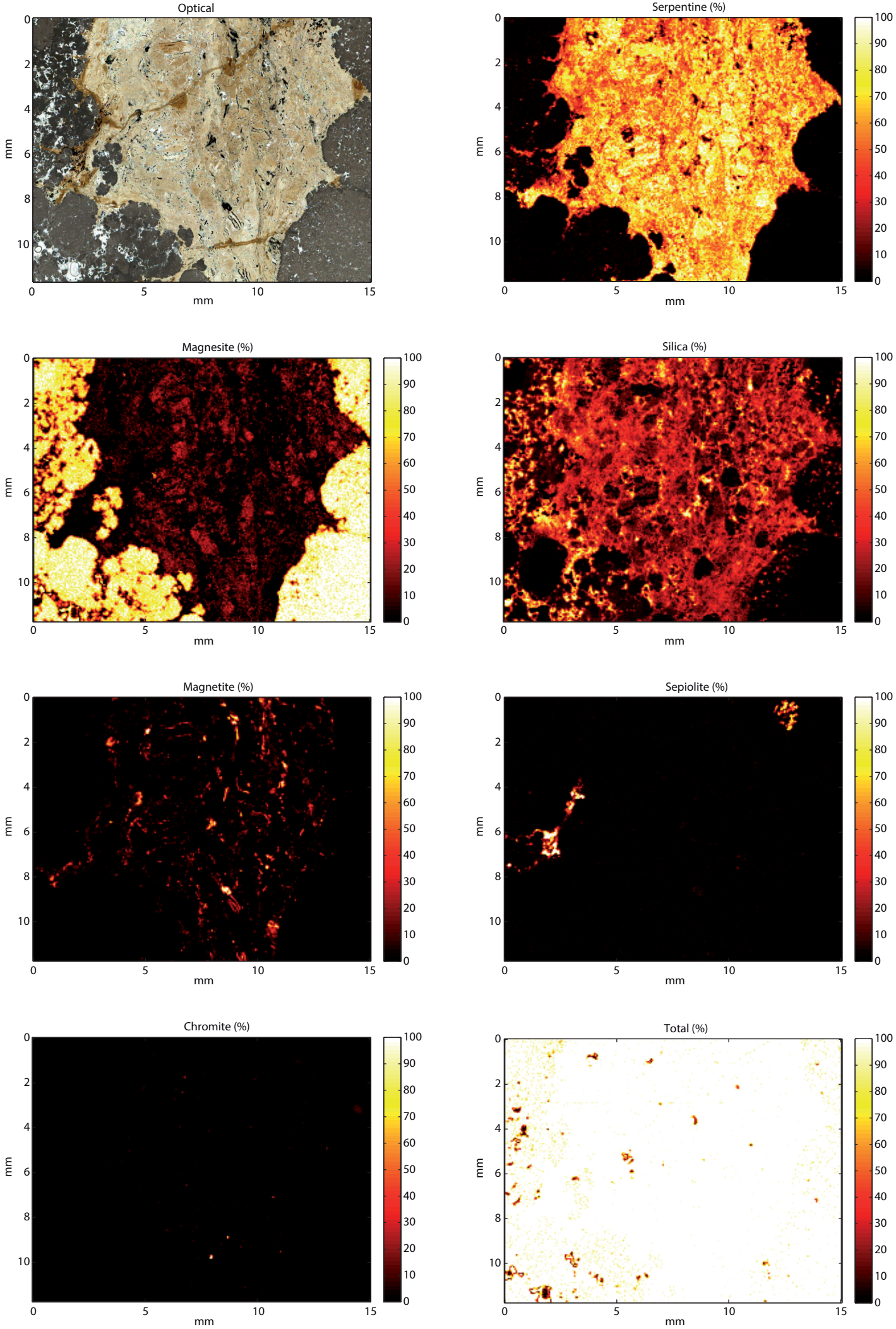
Optical
Serpentine (%)
Magnesite (%)
Silica (%)
Magnetite (%)
Sepiolite (%)
Chromite (%)
Total (%)
mm
0
2
4
6
8
10
5
10
15
100
90
80
70
60
50
40
30
20
10

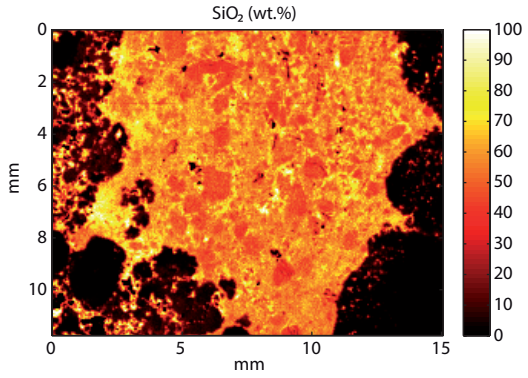
SiO2 (wt.%)
mm
mm

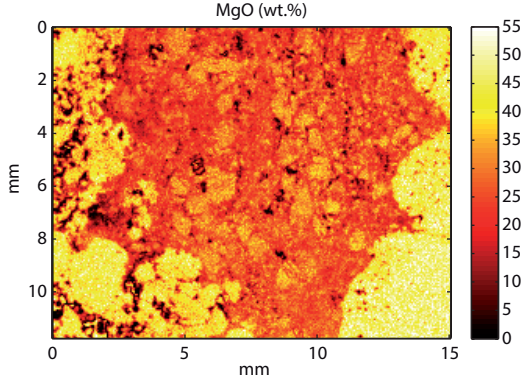
MgO (wt.%)
mm
mm

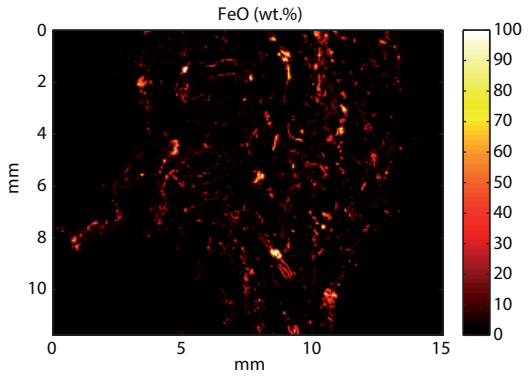
FeO (wt.%)
mm
mm

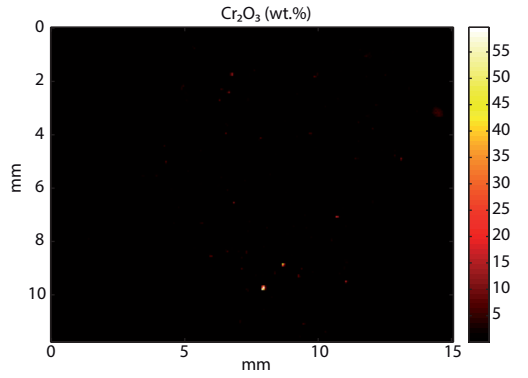
Cr2O3 (wt.%)
mm
mm

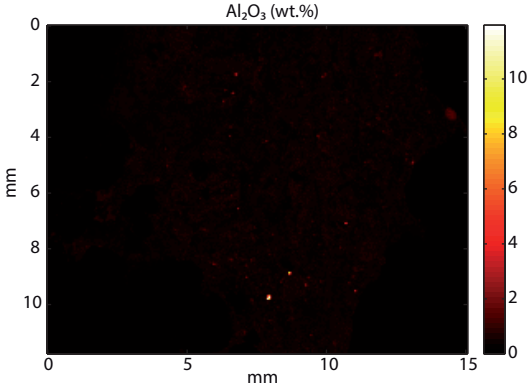
Al2O3 (wt.%)
mm
mm

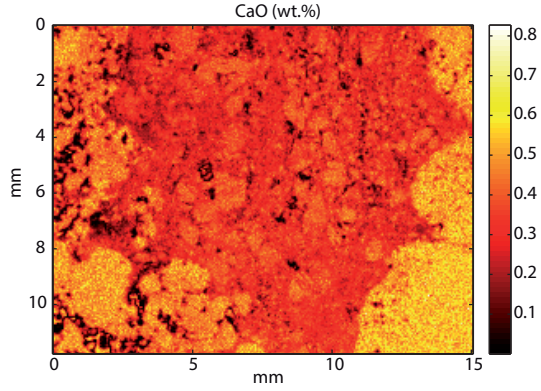
CaO (wt.%)
mm
mm

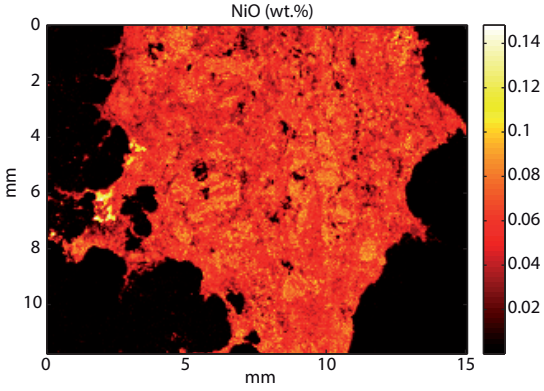
NiO (wt.%)
mm
mm

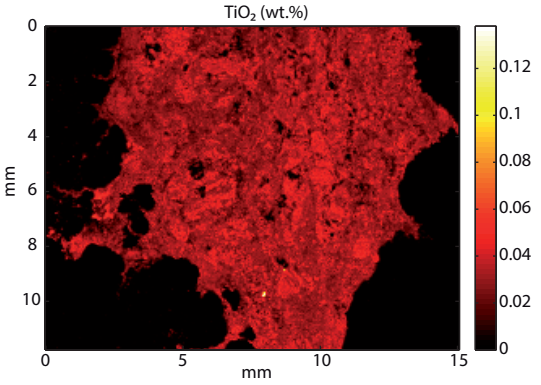
TiO2 (wt.%)
mm
mm

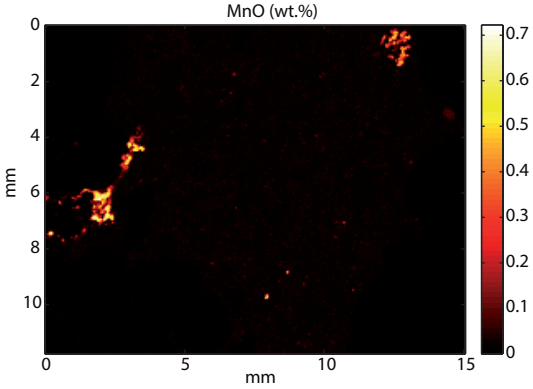
MnO (wt.%)
mm
mm

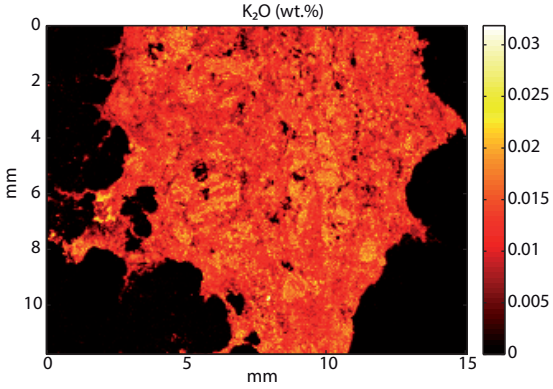
K2O (wt.%)
mm
mm

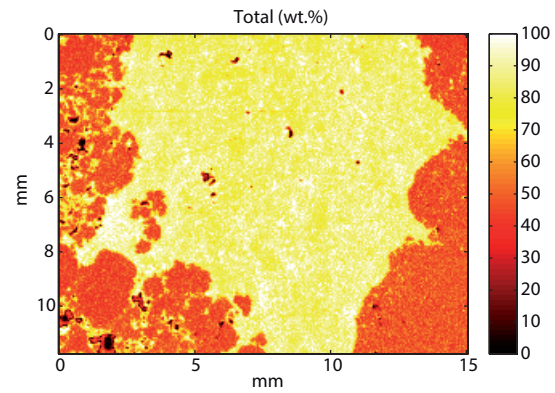
Total (wt.%)
mm
mm

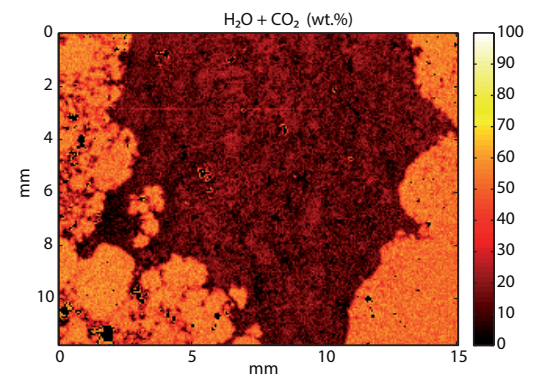
H2O + CO2 (wt.%)
mm
mm